Ion-beam manipulation and liquid-droplet dynamics in a vacuum explored with the aid of computational approaches

飯田, 岳史

Ion-beam manipulation and liquid-droplet dynamics in a vacuum explored with the aid of computational approaches

真空中のイオンビーム制御と液滴ダイナミクスの探究：計算機活用による実験支援

Doctoral Dissertation

TAKEFUMI HANDA

Graduate School of Science

Kyushu University

2024

Abstract

Computational science, also known as scientific computing, uses advanced computing capabilities to understand complex chemical and physical problems. Recent advancements in computer performance have substantially broadened the applicable fields: quantum chemistry, reaction kinetics, molecular dynamics, machine learning, optics, ion and electron beams, etc. This research aims to provide novel computer assisted approaches to ion-beam manipulation and liquid-droplet dynamics that are of particular interest in a vacuum. In the first part, the author developed an ion reflector for a mass spectrometer with a novel design improving ion-beam convergence, based on computational solutions of Laplace's equation. The numerical approach was extended further to establishing a methodology for analyzing spatial distribution of ions stored in a linear ion trap. In the second part, the author tackled the problems of water droplets in a vacuum by means of spectroscopy and imaging experiments, employing computational approaches to the Mie theory, Navie‐Stokes equations, machine learning, and image processing to extract properties of water in the supercooled state during rapid evaporative cooling. The implications of this research extend beyond the immediate scope, offering valuable insights into computer assisted studies.

Table of contents

Chapter 1. General introduction

Gas phase spectroscopy of isolated clusters is widely employed to measure their chemical properties. In particular, size selected clusters have been of interest as their properties exhibit non-scalability with the number of constituent atoms or molecules. Photodissociation [1–3] and photoelectron spectroscopy [4–10] gives insights into stability and geometry of the clusters. Major techniques in experiments are laser spectroscopy, mass spectrometry, and ion beams and traps.

Photodissociation spectroscopy is based on the development of ionization and ion-trap techniques as well as mass spectrometry. Major ionization techniques are electron impact [11], magnetron sputtering [12], matrix-assisted laser desorption/ionization (MALDI) [13, 14], and electrospray ionization (ESI) [15, 16]. Ionized clusters or molecules are accumulated and thermalized in ion traps. Among the versatile traps, linear multipole ion traps developed by Gerlich [17] have been making significant contribution in molecular physics. The combination of a linear multipole ion trap and a reflectron time-of-flight mass spectrometer [18] has been proven to be very useful in photodissociation spectroscopy.

More recently, evaporative cooling of liquids in a vacuum has emerged as a powerful technique for novel studies of supercooled liquids [19–21]. In these experiments, a laminar liquid jet was employed to generate 6–12 μm diameter water droplets in the estimated temperature of 230 to 250 K. From diffraction of femtosecond X-ray laser pulses [19] and Raman spectra of the OH stretching mode [21], ice formation is reported in the supercooled regime (at homogeneous ice nucleation temperature).

Today's personal computers have processing speed that exceeds the "SX-3" supercomputer (NEC Corp. in 1989) by more than 30 times. The semiconductor

industry's commitment to "Moore's Law" has resulted in significant acceleration to the increasing rates of transistor integration. G. Moore passed away in March 2023. Computational chemistry has experienced remarkable growth with the enhanced performance of computers. Notably, various studies carried out by quantum-chemical calculations, molecular-dynamics simulations, and machine-learning approaches are presented in conferences of the Chemical Society of Japan. There are numerous frontiers yet to be explored, for example, analytically unsolvable problems like those in ion optics, Mie theory, etc.

For advancing these gas phase investigation, the present doctoral research took advantages of computer science as well as experimental techniques such as Raman spectroscopy and a high-speed camera. The dissertation is organized by five distinct chapters in two major parts, each of which is addressing a specific facet of the research. Chapter 2 in the first part describes development of a reflectron time-of-flight mass spectrometer with a novel design to achieve a high detection efficiency required for photofragmentation spectroscopy of size selected clusters (Figure 1-1). The design is conceptualized by demonstrating its performance for Ag_3^+ extracted from a linear ion trap. In Chapter 3, numerical ion-beam simulation is presented for predicting a spatial ion distribution in linear multipole traps (Figure 1-2). With the recent up-graded CPU (central processing unit), it is now feasible to compute the distribution of ions near the space charge limit. Roland Glowinsk, known in the field of computational science of partial differential equations, emphasizes the importance of validation of numerical results based on experimental data [22]. This dissertation also places utmost importance on the validation and reproducibility of computational simulations based on experiments. The numerical results of ion distributions were validated by comparing with the results of

tomography measured by photofragmentation [23]. In the latter part, Chapters 4 and 5 show the dynamics of water droplets in a vacuum (Figure 1-3). Quadrupole oscillation induced upon droplet generation was observed, allowing detection of changes both in surface tension and in viscosity due to supercooling. The shrinking sizes of evaporatively cooled water droplets were probed by whispering gallery modes (WGMs) observed in the OH stretching band of water in the Raman scattering spectrum. Subsequent freezing events were investigated by a high speed camera, leading to discussion on the homogeneous ice nucleation rate and the process of ice-crystal growth. Evaporative cooling in a vacuum induces fragmentation of water droplets of 40 μm in diameter, which is in contrast to the prediction of the model calculation that less than 50 μm would not fragment [24]. Finally, Chapter 6 demonstrates that the precision of the droplet-size measurement via WGMs can be enhanced further by employing multiplex coherent anti-Stokes Raman scattering, which enables observation of multiple WGM signals in a broadband.

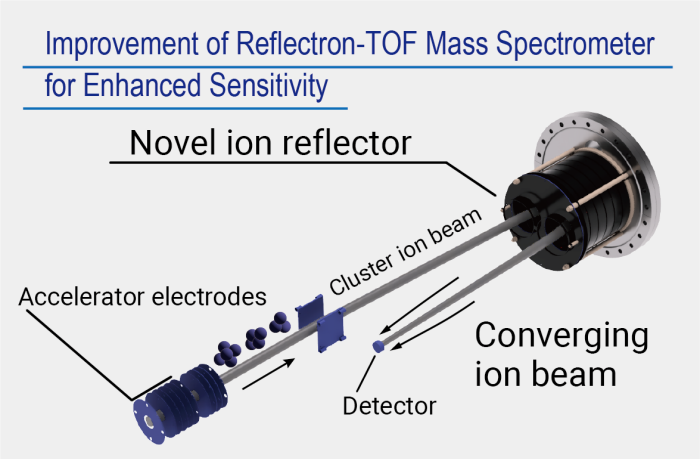

Figure 1-1. Conceptual graphics of the improved reflectron time-of-flight mass spectrometer. (Chapter 2)

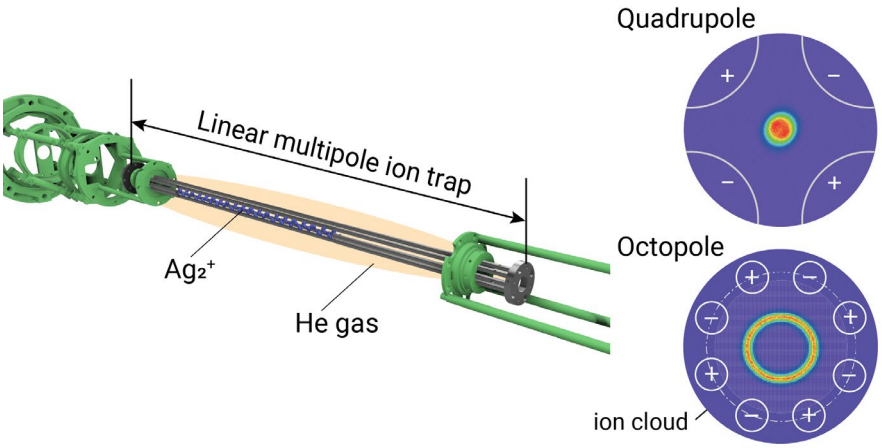

Figure 1-2. Graphical abstract of spatial distribution of ions in linear pole traps near space charge. (Chapter 3)

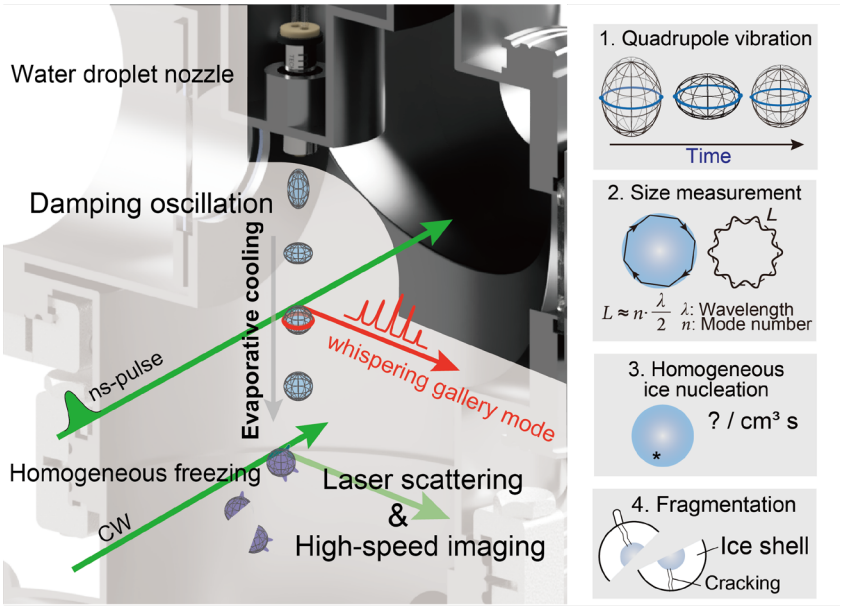

Figure 1-3. A schematic showing dynamics of water droplets evaporatively cooled in a vacuum. (Chapter 4,5)

References

1. M. A. Johnson, M. L. Alexander, and W. C. Lineberger, *Chem. Phys. Lett.* **112**, 285 (1984). doi: 10.1016/0009-2614(84)85742-5
2. W. A. Saunders, P. Fayet, and L. Wöste, *Phys. Rev. A* **39**, 4400 (1989). doi: 10.1103/PhysRevA.39.4400
3. R. Schäfer and J. A. Becker, *Phys. Rev. B* **54**, 10296 (1996). doi: 10.1103/PhysRevB.54.10296
4. O. Cheshnovsky, K. J. Taylor, J. Conceicao, and R. E. Smalley, *Phys. Rev. Lett.* **64**, 1785 (1990). doi: 10.1103/PhysRevLett.64.1785
5. G. Ganteför, M. Gausa, K-H. Meiwes-Broer, and H. O. Lutz, *J. Chem. Soc. Faraday Trans.* **86**, 2483 (1990). doi: 10.1039/FT9908602483
6. A. Nakajima, T. Taguwa, K. Hoshino, T. Sugioka, T. Naganuma, F. Ono, K. Watanabe, K. Nakao, Y. Konishi, R. Kishi, and K. Kaya, *Chem. Phys. Lett.* **214**, 22 (1993). doi: 10.1016/0009-2614(93)85449-X
7. J. Akola, M. Manninen, H. Häkkinen, U. Landman, X. Li, and L. S. Wang, *Phys. Rev. B* **62**, 13216 (2000). doi: 10.1103/PhysRevB.62.13216
8. D. M. Neumark, *Annu. Rev. Phys. Chem.* **52**, 255 (2001). doi: 10.1146/annurev.physchem.52.1.255
9. J. V. Coe, S. M. Williams, and K. H. Bowen, *Int. Rev. Phys. Chem.* **27**, 27 (2008). doi: 10.1080/01442350701783543
10. L. Ma, K. Majer, F. Chirot, and B. von Issendorff, *J. Chem. Phys.* **131**, 144303 (2009). doi: 10.1063/1.3245859
11. J. E. Pollard and R. B. Cohen, *Rev. Sci. Instrum.* **58**, 32 (1987).

doi: 10.1063/1.1139562

12. H. Haberland, M. Karrais, M. Mall, and Y. Thurner, *J. Vac. Sci. Technol. A* **10**, 3266 (1992). doi: 10.1116/1.577853
13. K. Tanaka, H. Waki, Y. Ido, S. Akita, Y. Yoshida, and T. Yoshida, *Rapid Commun. Mass Spectrom.* **2**, 151 (1988). doi: 10.1002/rcm.1290020802
14. M. Karas and F. Hillenkamp, *Anal. Chem.* **60**, 2299 (1988). doi: 10.1021/ac00171a028
15. C. M. Whitehouse, R. N. Dreyer, M. Yamashita, and J. B. Fenn, *Anal. Chem.* **57**, 675 (1985). doi: 10.1021/ac00280a023
16. J. G. Boyle and C. M. Whitehouse, *Anal. Chem.* **64**, 2084 (1992). doi: 10.1021/ac00042a011
17. D. Gerlich, *Adv. Chem. Phys.* **82**, 1 (1992). doi: 0.1002/9780470141397.ch1
18. B. A. Mamyrin, V. I. Karataev, D. V. Shmikk, and V. A. Zagulin, *Sov. Phys. JETP* **37**, 45 (1973).
19. J. A. Sellberg, C. Huang, T. A. McQueen, N. D. Loh, H. Laksmono, D. Schlesinger, R. G. Sierra, D. Nordlund, C. Y. Hampton, D. Starodub, D. P. Deponte, M. Beye, C. Chen, A. V. Martin, A. Barty, K. T. Wikfeldt, T. M. Weiss, C. Caronna, J. Feldkamp, L. B. Skinner, M. M. Seibert, M. Messerschmidt, G. J. Williams, S. Boutet, L. G. M. Pettersson, M. J. Bogan, and A. Nilsson, *Nature* **510**, 381 (2014). doi: 10.1038/nature13266
20. H. Laksmono, T. A. McQueen, J. A. Sellberg, N. D. Loh, C. Huang, D. Schlesinger, R. G. Sierra, C. Y. Hampton, D. Nordlund, M. Beye, A. V. Martin, A. Barty, M. M. Seibert, M. Messerschmidt, G. J. Williams, S. Boutet, K. A. Winkel, T. Loerting, L. G. M. Pettersson, M. J. Bogan, and A. Nilsson, *J. Phys. Chem. Lett.* **6**, 2826 (2015).

doi: 10.1021/acs.jpclett.5b01164

21. C. Goy, M. A. C. Potenza, S. Dedera, M. Tomut, E. Guillerm, Anton Kalinin, K. Voss, A. Schottelius, N. Petridis, A. Prosvetov, G. Tejeda, J. M. Fernández, C. Trautmann, F. Caupin, U. Glasmacher, and R. E. Grisenti, *Phys. Rev. Lett.* **120**, 015501 (2018). doi: 10.1103/PhysRevLett.120.015501
22. M-O. Bristeau, G. Etgen, W. Fitzgibbon, J. L. Lions, J. Périaux, and M. F. Wheeler (Ed.), Computational Science for the 21st century, 1st ed., Wiley Press, 1997.
23. T. Majima, G. Santambrogio, C. Bartels, A. Terasaki, T. Kondow, J. Meinen, and T. Leisner, *Phys. Rev. A* **85**, 053414 (2012). doi: 10.1103/PhysRevA.85.053414
24. S. Wildeman, S. Sterl, C. Sun, and D. Lohse, *Phys. Rev. Lett.* **118**, 084101 (2017). doi: 10.1103/PhysRevLett.118.084101

Part 1

Gas-phase ion-beam techniques for cluster science

Chapter 2. Reflectron time-of-flight mass spectrometer for improved convergence of ion beam

2-1. Introduction

Time-of-flight mass spectrometry is widely employed for mass analysis of various ions ranging from small molecules to large substances. Its advantages over other mass spectrometers are short acquisition time of measurement and no theoretical mass limit. A TOF mass spectrometer (TOF-MS) is combined with various ionization techniques such as multi-photon ionization [1], electron impact [2], matrix-assisted laser desorption/ionization (MALDI) [3,4], and electrospray ionization (ESI) [5,6]. The basic principle is that ions accelerated by the same electric potential travel at velocities dependent on their mass-to-charge ratio, m/q. The ratio can be determined by measuring their arrival times at an ion detector, which is proportional to $(m/q)^{1/2}$.

A typical TOF-MS employs a two-stage extraction field for ions, so called the Wiley-McLaren configuration [7], which compensates for the arrival time dispersion caused by ions distributed in a finite volume in the first extraction field. This is known as "space-focusing," which improves mass resolving power significantly. Space-focusing condition can be optimized by adjusting the potential difference between the two extraction fields. Once the space-focusing condition is optimized, one can further improve mass resolving power by an ion reflector proposed by Mamyrin et al. [8], where ions are reflected so that the arrival-time dispersion caused by initial kinetic-energy distribution of ions is compensated for by "energy-focusing." Among various types of ion-extraction electrodes and ion reflectors developed so far [9], most of high-resolution

TOF-MSs employ the Wiley-McLaren configuration combined with Mamyrin's ion reflector, which is known as a reflectron TOF mass spectrometer (RTOF-MS).

It should be noted that an ion reflector itself causes diverging ion trajectories. In conventional designs of RTOF-MSs, the electric field created in an ion reflector has a cylindrical symmetry, where the symmetry axis is tilted with respect to an incoming ion beam to reflect the ions to an ion detector. Here, ions with dispersed kinetic energies pass through different trajectories as high-energy ions penetrate deeper in the ion reflector than low-energy ones. Therefore, ions that extremely spread over a large volume in the first ion-extraction region could reach out of the detector due to their significantly dispersed kinetic energies, as described in detail in the next section. Note that, to the best of our knowledge, this problem has not been addressed before because the initial ion volume in conventional RTOF-MSs is usually arranged to be small so as to achieve high mass resolution, which allows all the ions to reach the detector.

In the present study, we develop a novel ion reflector that improves convergence of energetically spread ion beams to overcome this problem in conventional RTOF-MSs. Our new ion reflector has an electrostatic lens in front of a conventional grid-less ion reflector [10] for converging ion beam on a detector. The ion lens consists of a metal plate with two through-holes and an eyeglasses-frame electrode, allowing both incoming and outgoing beams to pass through the center of the apertures of the lens, where an ideal electric field is formed. We note that, although combination of an electrostatic lens with a grid-less ion reflector has been reported by Scherer et al. for steering an ion beam toward a detector [11], our design and objective are totally different from theirs. Here we aim at efficient detection of large-volume ions, extending previous studies on linear TOF-MSs [12–14] to RTOF-MS.

2-2. Ion-trajectory simulations

A conventional ion reflector

First we demonstrate divergence of an ion beam caused by a conventional ion reflector using ion-trajectory simulation. We performed trajectory simulations by SIMION8.0 software [15], assuming RTOF-MS equipped with a Wiley-McLaren-type ion accelerator and a grid-less ion reflector as shown in Figure 2-1. A MCP (Micro-Channel Plate) with an effective diameter of 14.5 mm was assumed as an ion detector. We deal with silver cluster ions for the present demonstration. Fifty ions of one of the isotopologues of Ag_3^+ were randomly generated at initial velocities of zero in a volume as large as 1.8 cm^3, i.e., a cylinder with 12-mm diameter and 16-mm length, in the first stage of the accelerator (the ion-extraction region). Voltages applied to the acceleration electrodes and the ion reflector were optimized as such that flight times of two ions separated by 11 mm along the flight path in the ion-extraction region were within 0.01 ms. Note that grid-less ion-extraction electrodes proposed by Sarugaku et al. [14] for linear TOF-MS did not provide sufficiently high mass resolution in RTOF-MS probably because the energy spread of the ions was too large to be compensated for by a reflectron. Therefore, the present ion-extraction electrodes are with a mesh both in the simulation and in the experiment described later. Ion trajectories thus calculated are shown in Figure 2-1(a); the ion beam significantly diverges after exiting the ion reflector, which degrades the efficiency of ion detection at the MCP.

The reason for this divergence is explained by Figure 2-2, which shows a cross-sectional view of calculated equipotential surfaces around the ion reflector of Figure 2-1(a). It is evident from this figure that the electric-field gradient in front of the ion

reflector (the blue-shadowed region) causes the ion beam to be dispersed due to kinetic-energy difference when the ion-beam path is off the axis of the cylindrical symmetry of the ion reflector (the dash-dot line in Figure 2-2). On the other hand, one expects that the ion beam converges by the electric-field gradient upon leaving the ion reflector if it passes along the axis of the cylindrical symmetry, which is the key finding in the present simulation for our design of a new ion reflector.

A new ion reflector

Figure 2-3 shows a schematic view of a new ion reflector designed in this study. Novel features of this reflector are (a) an eyeglasses-frame electrode and (b) an electrode with two through-holes mounted in front of (c) a stack of reflecting electrodes. While the electrode with two through-holes is grounded, the eyeglasses-frame electrode is negatively/positively biased for positively/negatively charged ions. This configuration creates two ion lenses working both for incoming and for outgoing ions, which allows the outgoing ion beam to converge on a detector. The inner diameters of the lens electrodes (a) and (b) are assumed to be 65 mm, which is the largest possible size for the reflecting electrodes (c) with an inner diameter of 140 mm; the large lens aperture has an advantage in introducing laser or X-ray beam for spectroscopic applications.

The performance of the new reflector is examined by creating a 3D model shown in Figure 2-4(a) based on our setup [16]; we suppose to replace our current ion reflector with the new one. We simulated ion trajectories repeatedly to optimize voltages applied to the accelerator, einzel lens, deflectors, and the new ion reflector. The same initial volume of an ion cloud was assumed in the extraction region that employed in the simulation of Figure 2-1. As many as 10,000 ions were randomly generated with zero

velocity in this case to critically examine the performance of the new reflector by producing a TOF histogram. The calculated ion trajectories are shown in Figures 2-4(b) and (c), which are 2D projections from the X- (a top view) and Y-axis (a side view), respectively, in Figure 2-4(a). All the ions are successfully converged on the MCP with an effective diameter of 14.5 mm as shown in Figure 2-4(d). Figures 2-4(e) and (f) show cross-sectional views of the calculated equipotential surfaces formed by the ion reflector. Unlike Figure 2-2, the divergence of the ion beam outgoing from the reflector is significantly suppressed by the local electric-field gradient formed in front of the reflector. The present simulation showed that the greenish region in Figures 2-4(e) and (f) is the electric-field gradient inherent to the eyeglasses-frame electrode, which works for the ion beam to converge in the X (vertical) direction, whereas the blue regions due to the grounded electrode work for convergence both in the X (vertical) and Y (horizontal) directions.

We further examined effects of the eyeglasses-frame electrode and the aperture diameter of the additional lens as shown in Figure 2-5. Figure 2-5(a) replicates Figure 2-4(d), showing spatial distribution of ions on the MCP detector calculated for the present configuration of the ion reflector illustrated in Figure 2-3. Figure 2-5(b) shows ion distribution obtained for a configuration without the eyeglasses-frame electrode, where ions undergo significant divergence in the X direction. Both the two through-holes and eyeglasses-frame electrodes are thus essential to guide all the ions to the detector. On the other hand, Figure 2-5(c) shows the case where the diameter of the lens apertures is reduced from 65 to 45 mm. The ion distribution of Figure 2-5(c) is almost the same as Figure 2-5(a), indicating that the size of the lens aperture does not have much influence on the ion detection efficiency.

2-3. Experimental procedure

We built a new reflector shown in Figure 2-6 based on the results of simulation. The inner diameters of the lens electrodes and the reflecting electrodes of the reflector are 65 and 140 mm, respectively, as assumed in the simulation. The six pieces of cylindrical electrodes ((c) in Figure 2-6) are stacked with ruby balls (3 mm in diameter) in between for electric insulation, while the electrodes are connected by a chain of 10-MΩ resistors. The electrode (d), which has a 37-mm-diameter through-hole for introducing laser beams or synchrotron radiation, is placed on a PEEK base to make it electrically isolated from a mounting flange (not shown in Figure 2-6). All the electrodes are coated with fine graphite for preventing static charge.

After implementing the new ion reflector in our RTOF-MS, we examined its performance using silver trimer ions, Ag_3^+. The details of our setup for metal-cluster experiment have been described elsewhere [16]. Briefly, silver clusters are generated by a magnetron-sputter cluster-ion source cooled by liquid nitrogen [17,18]. Ag_3^+ ions size-selected by a quadrupole mass filter are transported through radio-frequency octopole ion guides and quadrupole deflectors, and are admitted to a 30-cm-long linear ion trap filled with a buffer helium gas (0.2 Pa). The Ag_3^+ ions thus stored are ejected from the ion trap by a pulsed voltage operating at 1 Hz to be introduced into the RTOF-MS. The ejected ions are injected into the ion-extraction region of TOF collinearly to the flight path of the ions, i.e., from left to right in Figure 2-4(a). The distance between the two extracting electrodes is 20 mm; the electrode plates are with a 20-mm diameter through-hole attached with a 78%-transmittance metal mesh. The ions are thus distributed in a cylinder of 20-mm diameter and 20-mm length (a volume of 6.3 cm^3) in

the beginning of acceleration. The accelerated ions are detected after folded back from the ion reflector to measure a TOF spectrum and a spatial profile of the ion beam. For spatial-profile measurement, the ions are detected by a MCP coupled with a phosphor screen (F1217-01, Hamamatsu Photonics KK, 40-mm effective diameter) to capture 2D images of ions by a digital camera. For TOF-spectrum measurement, on the other hand, a fast-response MCP (F4655-14, Hamamatsu Photonics KK, effective diameter 14.5 mm) is employed to evaluate mass-resolving power.

2-4. Experimental results

Figure 2-7(a) shows a typical 2D image of Ag_3^+ on the phosphor screen. The ions are successfully converged on the MCP detector as manifested in the image. The intensity profiles along X and Y axes are shown in Figures 2-7(b) and 7(c), respectively, which have nearly Gaussian profiles with a full-width at half-maximum (FWHM) of less than 10 mm. We thus succeeded in demonstrating an advantage of the novel ion reflector, which enables convergence of ions initially spread over a volume as large as 20 mm × 20 mm × 20 mm in space.

On the other hand, the blue solid line in Figure 2-8 shows a TOF spectrum of Ag_3^+ measured by using the fast-response MCP. Four peaks of isotopologues originating from silver isotopes (^{107}Ag and ^{109}Ag) are clearly resolved. Multiple-peak fitting of the spectrum assuming Gaussian profiles yielded mass resolution ($M/\Delta M$) of about 600. The green dashed line in Figure 2-8 presents a TOF histogram of 10,000 Ag_3^+ calculated by the ion trajectory simulations mentioned in Section 2.2, where the isotope ratio between ^{107}Ag and ^{109}Ag (0.5184 and 0.4816, respectively) was taken into account. The good

agreement between the measured and calculated TOF spectra indicates that our new RTOF-MS works as designed. It is also simulated that the mass-resolving power would be as high as $M/\Delta M \approx 1800$ if the initial volume of ions in the extraction region be a sphere of 1 mm in diameter.

2-5. Conclusion

A novel ion reflector for RTOF-MS was developed to improve convergence of an ion beam. The new reflector has two features: (1) two apertures providing separate beam paths for incoming and outgoing ions and (2) an eyeglasses-frame electrode applying a bias voltage in front of the reflector. These features allow both incoming and outgoing ions to pass through the center of the apertures, where the equipotential surfaces are appropriately designed so as to materialize convergence of ion beams. We demonstrated that Ag_3^+ ions converge on an ion detector with a spot size less than 10 mm in FWHM, even when the initial volume of the ions in the TOF extraction region is as large as 6.3 cm^3 (a cylinder with 20-mm length × 20-mm diameter). The mass resolving power was demonstrated to be reasonably good as well. Our new RTOF-MS would be suited not only for mass analysis of ions extracted from an ion trap but also, for example, for photoionization mass spectrometry of molecules and clusters by unfocused vacuum ultraviolet (VUV) radiation [19].

References

1. For example, U. Boesl,, *J. Phys. Chem.* **95**, 2949 (1991).
2. J. E. Pollard and R. B. Cohen, *Rev. Sci. Instrum.* **58**, 32 (1987). doi: 10.1063/1.1139562
3. K. Tanaka, H. Waki, Y. Ido, S. Akita, Y. Yoshida, and T. Yoshida, *Rapid Commun. Mass Spectrom.* **2**, 151 (1988). doi: 10.1002/rcm.1290020802
4. M. Karas and F. Hillenkamp, *Anal. Chem.* **60**, 2299 (1988). doi: 10.1021/ac00171a028
5. C. M. Whitehouse, R. N. Dreyer, M. Yamashita, and J. B. Fenn, *Anal. Chem.* **57**, 675 (1985). doi: 10.1021/ac00280a023
6. J. G. Boyle and C. M. Whitehouse, *Anal. Chem.* **64**, 2084 (1992). doi: 10.1021/ac00042a011
7. W. C. Wiley and I. H. McLaren, *Rev. Sci. Instrum.* **26**, 1150 (1955). doi: 10.1063/1.1715212
8. B. A. Mamyrin, V. I. Karataev, D. V Shmikk, and V. A. Zagulin, *Sov. Phys.* – JETP **37**, 45 (1973).
9. U. Boesl, *Mass Spectrom. Rev.* **36**, 86 (2017). doi: 10.1002/mas.21520
10. S. Scherer, K. Altwegg, H. Balsiger, J. Fischer, A. Jäckel, A. Korth, M. Mildner, D. Piazza, H. Reme, and P. Wurz, *Int. J. Mass Spectrom.* **251**, 73 (2006). doi: 10.1016/j.ijms.2006.01.025
11. R. Frey, G. Weiss, H. Kaminski, and E. W. Schlag, *Z. Naturforsch.* **40a**, 1349 (1985). doi: 10.1515/zna-1985-1225
12. W. A. de Heer and P. Milani, *Rev. Sci. Instrum.* **62**, 670 (1991). doi: 10.1063/1.1142066
13. F. Chandezon, B. Huber, and C. Ristori, *Rev. Sci. Instrum.* **65**, 3344 (2002). doi: 10.1063/1.1144571

14. S. Sarugaku, M. Arakawa, and A. Terasaki, *Int. J. Mass Spectrom.* **414**, 65 (2017). doi: 10.1016/j.ijms.2017.01.003

15. D. J. Manura and D. A. Dahl, SIMION 3D Version 8.0, Scientific Instrument Services, Inc. (2008).

16. S. Sarugaku, M. Arakawa, T. Kawano, and A. Terasaki, *J. Phys. Chem. C*, **123**, 25890 (2019). doi: https://doi.org/10.1021/acs.jpcc.9b05117

17. A. Terasaki, T. Majima, and T. Kondow, *J. Chem. Phys.* **127**, 231101 (2007). doi: 10.1063/1.2822022

18. A. Terasaki, T. Majima, C. Kasai, and T. Kondow, *Eur. Phys. J. D* **52**, 43 (2009). doi: 10.1140/epjd/e2008-00274-0

19. T. Hayakawa, M. Arakawa, S. Kono, T. Handa, N. Hayashi, K. Minamikawa, T. Horio, and A. Terasaki, *Z. Phys. Chem.* **235**, 213 (2021). doi: 10.1515/zpch-2020-1668

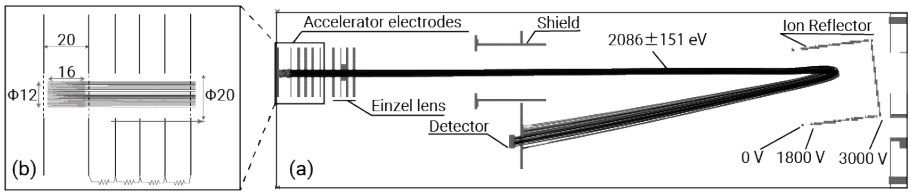

Figure 2-1. (a) A result of ion trajectory simulation of RTOF-MS equipped with a Wiley–McLaren ion accelerator and a conventional grid-less ion reflector. (b) An enlarged view of the accelerator: 50 ions were randomly generated in a cylinder of 12-mm diameter × 16-mm height in the extraction region. Only a part of the ions reaches the detector as the ions folded back by the ion reflector are diverging.

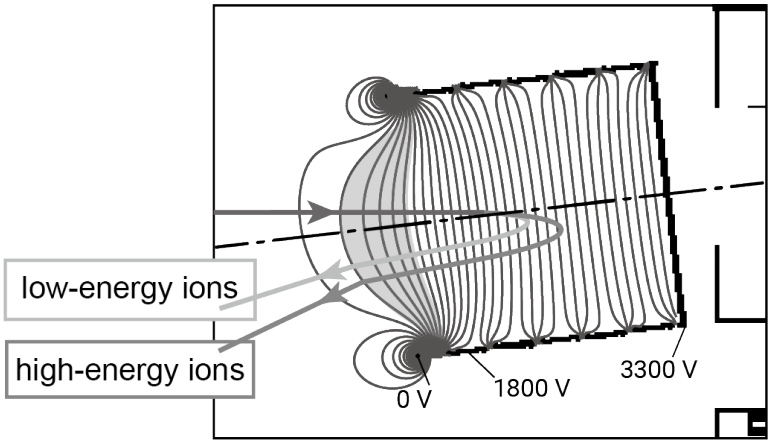

Figure 2-2. A cross-sectional view of calculated equipotential surfaces around the conventional ion reflector shown in Figure 2-1(a). It illustrates how the reflected ion beam diverges by the electric-field gradient formed in front of the reflector (the gray-shadowed region).

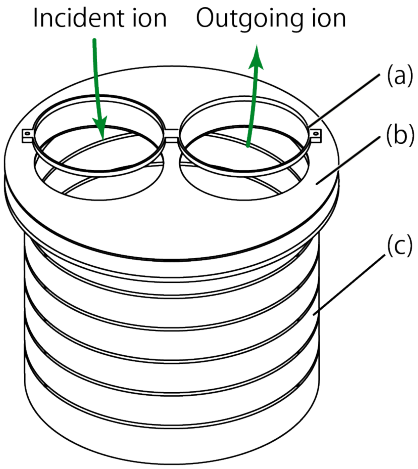

Figure 2-3. A schematic view of a new ion reflector designed in this study. (a) An eyeglasses-frame electrode. (b) A grounded electrode with two through-holes. (c) A stack of cylindrical electrodes.

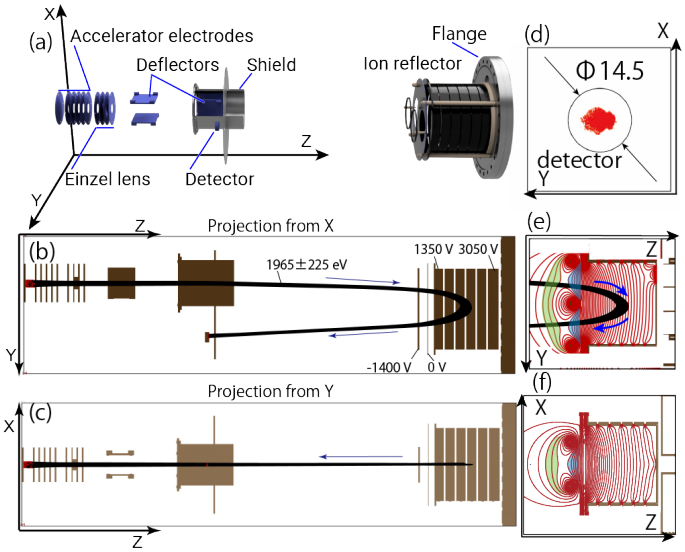

Figure 2-4. (a) A 3D model of the new RTOF-MS used in ion trajectory simulations. (b) and (c) Cross-sectional views of calculated ion trajectories from X (top view) and Y (side view) axes in Figure 2-4(a), respectively. (d) A 2D profile of ions on the MCP detector with 14.5-mm effective diameter. (e) and (f) Cross-sectional views of calculated equipotential surfaces around the new reflector.

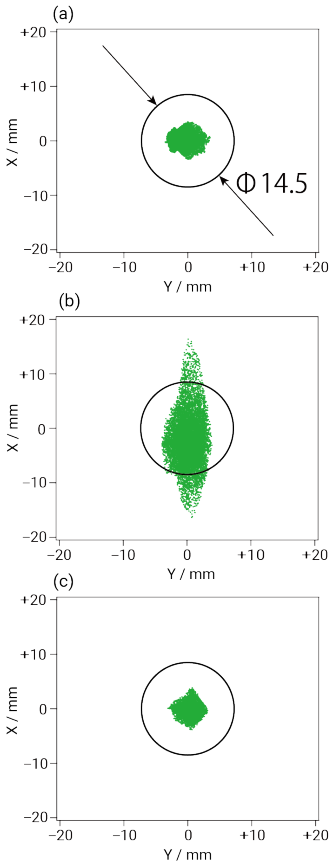

Figure 2-5. 2D profiles of ions on the MCP detector for different configurations of the ion reflector in RTOF-MS. (a) An original design of the ion reflector mounting a lens (a plate with two through-holes and an eyeglasses-frame electrode) with 65-mm diameter apertures. (b) An ion reflector without an eyeglasses-frame electrode. (c) An ion reflector with a size of lens apertures reduced to 45 mm.

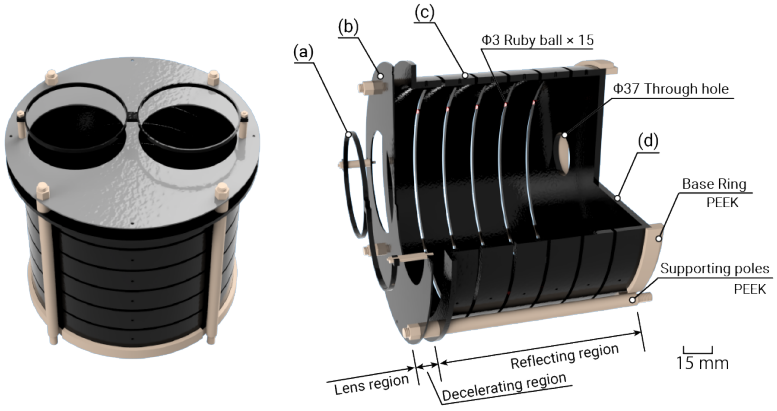

Figure 2-6. A rendered view of the new reflector built in this study. (a) An eyeglasses-frame electrode (SUS 304). (b) A grounded plate with two through-holes (A5052). (c) Cylindrical electrodes (A5052). (d) A base plate with a through-hole (A5052).

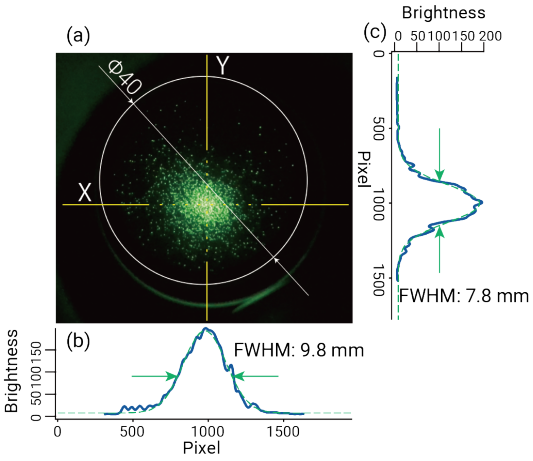

Figure 2-7. (a) A 2D image of Ag_3^+ ions detected by a MCP with a phosphor screen. (b) and (c) Solid lines: intensity profiles along X and Y, respectively. Dashed lines: Gaussian fitting curves.

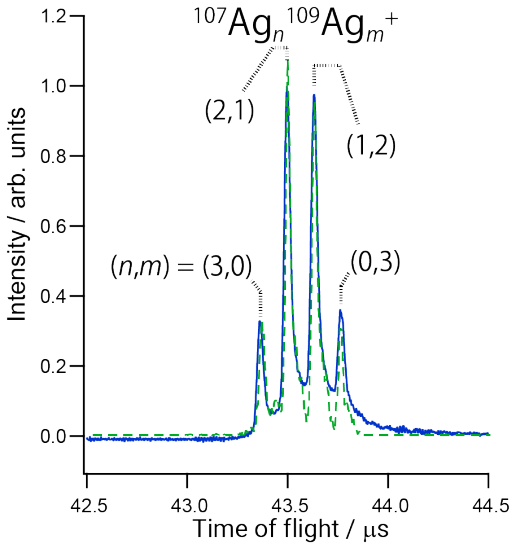

Figure 2-8. A TOF spectrum of isotopologues of Ag_3^+ ions. Blue solid curve: an experimental result. Green dashed curve: a TOF histogram obtained by simulation on 10,000 ions randomly created in the ion-extraction region of Figure 2-4(a). The natural isotope ratio was assumed for Ag isotopes.

Chapter 3. Ion trajectory simulation of trapped ions nearly at the space-charge limit

3-1. Introduction

Ion traps have been essential in chemical physics since the radio-frequency (rf) Paul trap [1] was developed. For 30 years, advancements in ion-trap techniques have given us versatile tools to explore physical and chemical properties of atoms, molecules and, clusters. Within those techniques, particularly noteworthy are the linear multipole rf ion traps by D. Gerlich [2], which have played a significant contributions in molecular physics. Linear multipole ion traps enable accumulation, temperature control and manipulation of ions for advanced spectroscopy [4-15], reaction-kinetics measurements [16-21], ultracold studies [22-25], etc.

In ion optics, linear multipole ion traps are one of the most elaborate systems. Manipulation of charged particles (ion optics) has been developed in the field of electron beams and ion mass spectrometry, where the pressure is so low, i.e., the mean free path is so long, that collisions between ions and background neutral atoms or molecules are negligible. On the other hand, in a linear multipole trap, about 0.1-Pa buffer gas is introduced to control the temperature [27] and to form an ion cloud in an equilibrated manner [28]. Helium is commonly chosen as the buffer gas, which is accessible down to cryogenic temperatures. The stored ions undergo various phases depending on temperature. At extremely low temperature, trapped atomic ions form a so-called Coulomb crystal, where the repulsion between ions is counterbalanced by the confinement imposed by the rf field [22,23]. As the temperature is raised, the Coulomb

crystal melts into an ion cloud due to collisions with the buffer gas. The spatial profile of the ion cloud is thus governed by the balance between the rf field, the buffer gas collisions, and the Coulomb repulsion. In particular, when ions are accumulated up to the space charge limit, repulsion between ions cannot be ignored.

In many applications of ion traps, it is important to characterize an ion-density profile in the trap because spatial distribution of ions have been found not to be uniform [29,30]. In photodissociation spectroscopy, for example, optimizing the alignment of the incident laser beam with the ion cloud is crucial for quantitative measurement of cross sections of optical responses. The discussion about dynamics of ions in a linear multipole rf trap has been explored by incorporating the effective potential of the rf field through the adiabatic approximation and the Coulomb repulsion by the mean-field approach [31]. Experimentally, an octopole trap is reported to have a ring-like ion distribution [29,32]. A comparable ring-type distribution has also been observed in a 12-pole trap [33]. In contrast, a quadrupole trap tends to locate the ions around the central axis of the trap [34-36].

In this research, we explore the ion distribution in a linear rf trap by ion trajectory simulation (SIMION [37]). The calculation of ion trajectories in rf multipole traps is computationally intensive. Therefore, certain approximations are employed. Specifically, Monte Carlo methods and Laplace's equation are utilized to address space charges, while a hard sphere collision model is applied to depict interaction among ions and buffer gas. This chapter demonstrates that the results obtained from SIMION are satisfactory for quantitative evaluation of ion distributions experimentally observed for a linear octopole trap at a high density of ions. Also, the simulation is consistent with an analytical prediction based on the adiabatic approximation [3,31], which assumes

pseudopotential [38] and thermal equilibrium. We report effects of the space charge and the temperature on the ion distribution in an octopole trap; the former is influenced by the amount of ions stored in the trap. An effect of the electrode structure is also discussed for a quadrupole trap. The present method can be applied to predicting spatial distribution of ions in the traps, even under space-charge-limit conditions, and also provides insights into ion temperature.

3-2. Computational procedures and conditions for ion cloud in traps by SIMION

A structure model of a linear octopole ion trap was created by referring to the experimental setup [9,39] as shown in Figure 3-1: the trap consists of 400 mm-long pole electrodes with 3 mm diameter, which were arranged in a cylindrical manner with 11 mm inscribed diameter, and two ring electrodes at both ends of the pole electrodes. The pole and ring electrodes were applied with rf and dc potentials for radial and axial confinement, respectively. The simulation space was defined using a potential array with a grid size of 0.2 mm, which was the minimum grid size available without exceeding the maximum number of grids (2×10^8) manageable in 32-bit SIMION 8.0. It is noteworthy that the maximum number of grids has been greatly improved to 2×10^{10} with SIMION8.1 with 64-bit support. Whatever the case, 0.2 mm grid size was sufficiently small not only to approximate a smooth cylindrical surface of the pole electrodes but also to well-reproduce the potential gradient inside the trap for calculation of ion trajectories. As for ions to trap, Ag_2^+ was assumed, which is characterized by an averaged mass of 216 u and a collisional cross section with a He gas of 3.25×10^{-19} m^2 that has been reported by ion mobility experiment [40]. The collision cross section was calculated from a van der Waals radius

or the Langevin collision theory in other report [44]. Although the collision cross section is expected to be energy dependent, it was assumed to be constant in the present simulations. The trap was driven by 3 MHz rf potentials with an amplitude of 200 V; its offset dc was adjusted to −12 V. An axial potential barrier was given by the ring electrodes biased at +10 V. These parameters were taken from the conditions of experiment reported previously [29]. In SIMION, a 3D potential array is calculated by solving the Laplace equation. It should be noted that the Laplace equation inherently cannot handle space charge because it is a special case of the Poisson equation, assuming zero space charge throughout the volume. Therefore, evaluation of space charge effects on the potential array requires solving the time-dependent Poisson equation, which is supported since SIMION8.1. However, for simulation of trapped ions in a time scale of hundreds of milliseconds, solving the Poisson equation remains computationally demanding. Alternatively, SIMION is implemented with a "charge repulsion" method. When enabled, it accounts for Coulomb's law-like "particle‑particle" forces. This method can be used to evaluate the spatial ion distribution in the ion trap. Note that this repulsion method assumes that the electric field from the electrodes is independent of and unaffected by the electric field from the space charge. Therefore, this method may not be valid in the cases where the space charge perturbs the electric field of electrodes [41,42], which is not the case for the present ion-trap simulation.

Among the charge repulsion methods, we employed "factor repulsion," which is statistical random sampling known as a Monte Carlo method. It can deal with time-dependent space-charge distribution [41,42]. The total charge, Q, of all the ions is expressed by multiplying a factor repulsion, f, to the number of groups of ions, N: $Q = f N$, which is given in the unit of the elementary charge, e. Accuracy of the Monte Carlo

method depends on the size of the sample. We have tried to find a reasonable value of N by performing simulation for several N values from 100 to 1,000 every 100. As we will discuss later, the ions in an octopole trap are found to form a ring-type ion cloud, where the diameter of the ring is regulated by the equilibrium between the repulsive force arising from space charge and the confinement by rf potential. Therefore, the diameter of the ion ring is plotted as a function of N, as shown in Figure 3-2. The ring diameter exhibited an increase as the N value varied from 100 to 500, whereas it leveled off above $N = 600$. In addition, FWHM (full width at half maximum) of the ion-ring thickness as a function of N is shown in Figure 3-3, which remained almost constant above $N = 300$. Therefore, we decided to perform trajectory simulations by fixing $N = 600$; for the total charge, Q, of 5.5×10^8 e, the factor repulsion, f, is 9.17×10^5 ($5.5 \times 10^5/600$).

The effect of buffer He gas collisions was taken into account by the hard-sphere collision model (HS1) that is useful for non-vacuum trajectory simulation [41,43]. This model calculates the collision probability and the momentum transfer expected for the experiment, where the temperature and the pressure were 300 K and 0.1 Pa, respectively. In the HS1 collision model, the He–ion collisions are considered to be elastic, where the velocity of the He atoms was assumed to follow the Maxwell–Boltzmann distribution. Here, the ion dynamics is separated into He–ion collisions and charge repulsion. In the collision model, the ion is treated as a hard sphere that is characterized by the collisional cross section of Ag_2^+ with a He gas [40]. In the "factor repulsion" method, each ion is assumed to act as a point charge, which actually represent a cloud of ions. SIMION compensates for the issue arising when the point charge is expanded into an ion cloud [41].

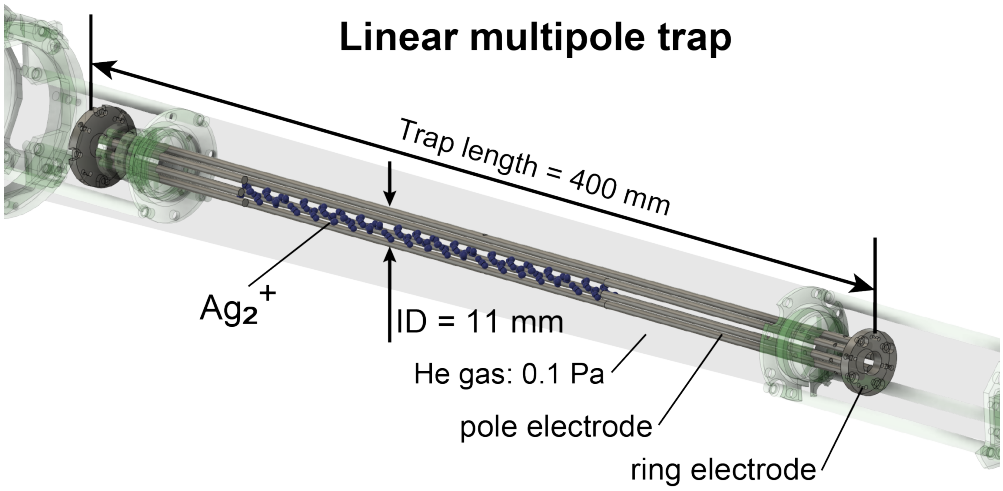

Figure 3-1. A schematic of an octopole ion trap with pole rf electrodes and ring dc electrodes for radial and axial confinement, respectively.

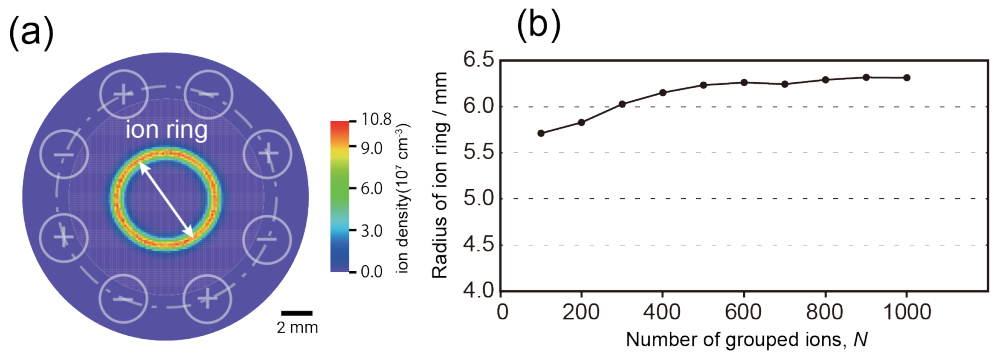

Figure 3-2. (a) The ion ring profile of ion distribution in a linear octopole trap. (b)The radius of the ring of an ion cloud as a function of the number of grouped ions, *N*, specified in the simulation of an octopole ion trap. The radius increases up to *N* = 600, above which it levels off.

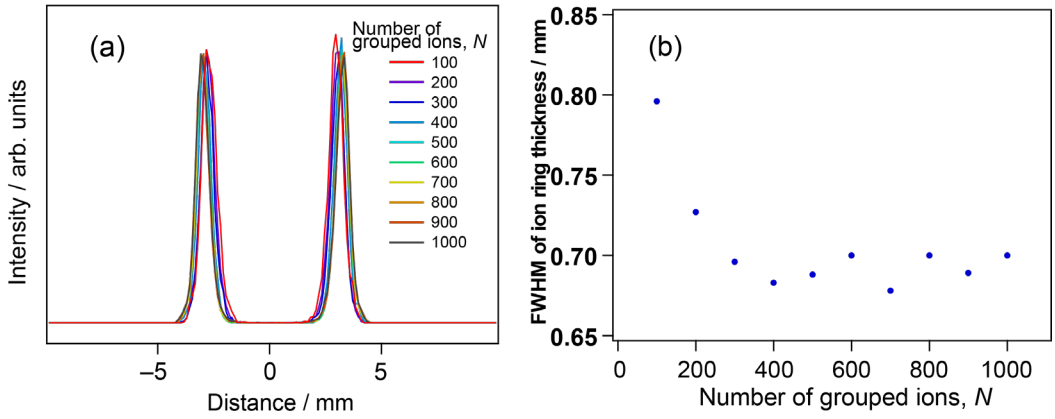

Figure 3-3. (a) Radial ion-distribution profiles across the center of the trap calculated at *T* = 300 K for various conditions of the number of grouped ions, *N*. The net amount of ions stored was 5.5×10^8, i.e., the trap is nearly at the space charge limit. (b) FWHM of the ion-ring thickness as a function of *N*, as derived from the results of (a). The FWHM values are almost the same for *N* > 300, rationalizing the validity of *N* = 600 employed in the present simulation based on the factor repulsion method.

3-3. Results and discussion

Octopole ion trap: simulation vs. experiment

A simulated spatial distribution of Ag_2^+ in an octopole ion trap is shown in Figure 3-4. An ion density is derived by normalizing the 900,000 data points of the grouped ions to the 5.5×10^8 ions indeed stored in the trap. Each bin width of the 2D histogram is 125 μm × 125 μm. The ion cloud was thus found to form a ring profile with a diameter of 6.3 mm in this particular case; the ring diameter depends on the total amount of ions.

To compare this result of the simulation with experiment, we should pay attention to the experimental procedure described in Ref. [29], where the ion density was probed by the photofragmentation technique. In this technique, a collimated laser beam with a diameter of 2 mm was irradiated collinearly to the trap axis, inducing fragmentation of Ag_2^+ to Ag^+. Since the signal of the fragmented Ag^+ is proportional to the local density of trapped ions, the ion-density profile was obtained by scanning the laser position both vertically and horizontally with an interval of 0.5 mm. Therefore, the result of the present simulation (Figure 3-4) should be convolved with a Gaussian function of 2 mm in FWHM representing the laser-beam profile. Figure 3-5(a) shows the result of simulation thus obtained after convolution with the Gaussian profile, which should be compared with the experimental result shown in Figure 3-5(b) reproduced from [29]. It should be noted that the absolute value of the ion density as well as the diameter and the thickness of the ion ring are well-reproduced quantitatively; the maximum ion density, the ion-ring diameter, and its thickness observed by the experiment are $3.0 \times 10^7/cm^3$, 7 ± 1 mm and 2.3 ± 0.2 mm, respectively, while they are $3.4 \times 10^7/cm^3$, 6.0 mm and 2.3 mm in the present

simulation.

If we take a closer look at the experimental result, a slight variation in the ion density is discernible along the ring, which was attributed to imperfect arrangement of the pole electrodes [29,30]. On the other hand, the result of simulation shows almost perfect cylindrical symmetry, representing an ideal case. In this context, we should note that the grid size of 0.2 mm, providing the spatial resolution of the present simulation, is sufficiently small to express the smooth surface of the pole electrodes. Note also that this simulation is consistent with an analytical prediction based on the adiabatic approximation [3,31]. The present success in reproducing the ion distribution measured experimentally confirms that the combination of the hard-sphere collision model and the charge-repulsion method in SIMION is appropriate for predicting an ion distribution in a linear rf ion trap even in high ion-density regions, where the space charge is essentially important.

Octopole ion trap: effects of the ion-loading amount, the rf amplitude, and the temperature

Ion distributions as a function of the number of trapped ions, the rf amplitude, and the temperature are further examined. When the number of ions in the octopole trap was reduced by one order of magnitude from 5.5×10^8 ions (1.4×10^7 ions/cm) to 5.5×10^7 ions (1.4×10^6 ions/cm), the diameter of the ion ring decreased from 6.3 (Figure 3-4) to 4.4 mm (Figure 3-6(a)). It would be worth mentioning that the thickness of the ion ring became larger at the lower amount of ions. This broadening of the ion cloud is due to the smaller gradient $\mathrm{d}\Phi/\mathrm{d}r$ of the effective potential at the radial position closer to the center of the trap: a smaller ion ring is predicted to be thicker.

The present simulation was extended even to a wider range of ion-trap conditions that can be compared with experiments [29]. Figure 3-7 shows dependence on the number of ions stored, i.e., 4.0×10^7, 1.6×10^8, and 1.1×10^9 ions, which are the same amount of ions that experiments were performed (Figure 3 of Ref. [29]). The ion-ring diameters and the values of the ion density are reproduced well. It is also discernible both in the experiment and in the present simulation that the dip in the ion-density profile at the center of the trap becomes more prominent as the ion-loading amount increases. Furthermore, Figure 3-8 presents dependence on the rf amplitude applied to the trap electrodes. The simulation is consistent with the experiment (Figure 4 of Ref. [29]) in that higher amplitude makes the ion ring smaller.

Figure 3-6(b) shows an ion distribution at a buffer He-gas temperature, T = 10 K, lower than that of Figure 3-6(a), T = 300 K, storing the same 5.5×10^7 ions in the trap. The thickness of the ion ring became thinner at the lower temperature, while the diameter remained the same. This temperature dependence suggests that the thickness of the ion ring is caused by thermal collisions of the buffer He gas. The ion ring at T = 10 K is indeed extremely thin, possessing only one pixel of width. This remarkable change in the ion-ring thickness upon cooling from 300 to 10 K is worth noting.

We should also note that the translational kinetic energy of the trapped ions is much higher than the thermal energy of the buffer He gas due to space charges. The space charge raises the translational temperature of the ions considerably, as discussed previously by simulation of kinetic ion temperature in a linear multipole trap [44]. The kinetic energy distribution under several space charge conditions are shown in Figure 3-9. The ion temperatures obtained from the kinetic-energy distributions are much higher than the temperature of the buffer He gas, i.e., the translational energy is not in

equilibrium with the buffer gas. Even with such high translational temperatures, the internal temperature of the ions, which is not available in the present simulation, is regulated by the buffer gas as demonstrated by temperature studies in spectroscopic experiments [39,45].

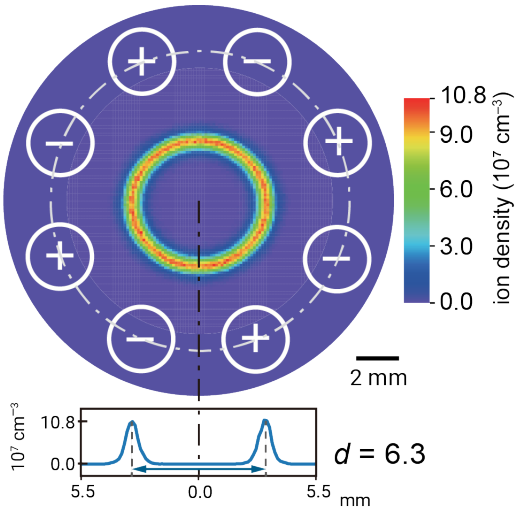

Figure 3-4. A 2D histogram of positions of ions simulated for an octopole trap. The coordinates of 600 grouped ions (N = 600) were accumulated for simulation time every 100 μs from 50 to 200 ms, creating 900,000 positions of ions as displayed. The charge repulsion parameter was equivalent to 5.5 × 10^8 singly-charged ions. The pressure and temperature of the buffer He gas were set to 0.1 Pa and 300 K, respectively. The lower panel shows the ion-density profile across the center of the trap.

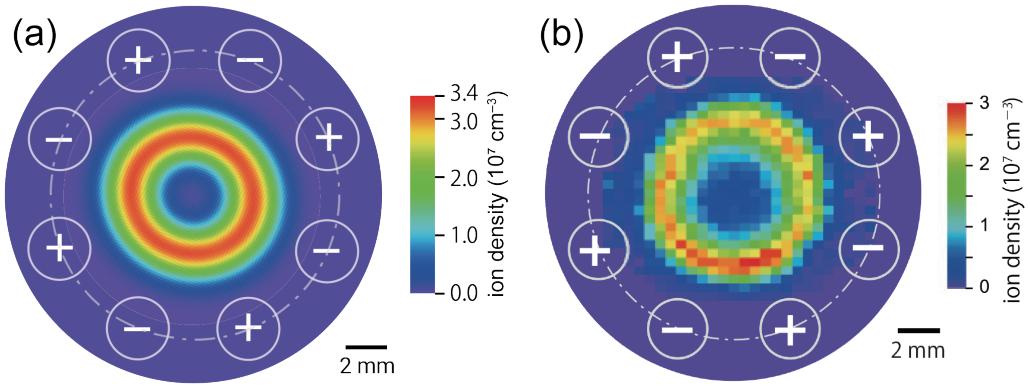

Figure 3-5. (a) A 2D histogram obtained from Figure 3-4 by convolution of a Gaussian profile (FWHM: 2 mm), which is to be compared with an experimental result shown in panel (b). The Gaussian profile represents a laser beam irradiated in the photofragmentation experiment. (b) A 2D distribution of Ag_2^+ ions that was measured by photofragmentation experiment to probe the local density of ions reported in Ref. [29]. The total number of ions in the trap was about 5.5 × 10^8 ions. Panel (b) is reproduced with permission from Ref. [29]. Copyright 2012 American Physical Society.

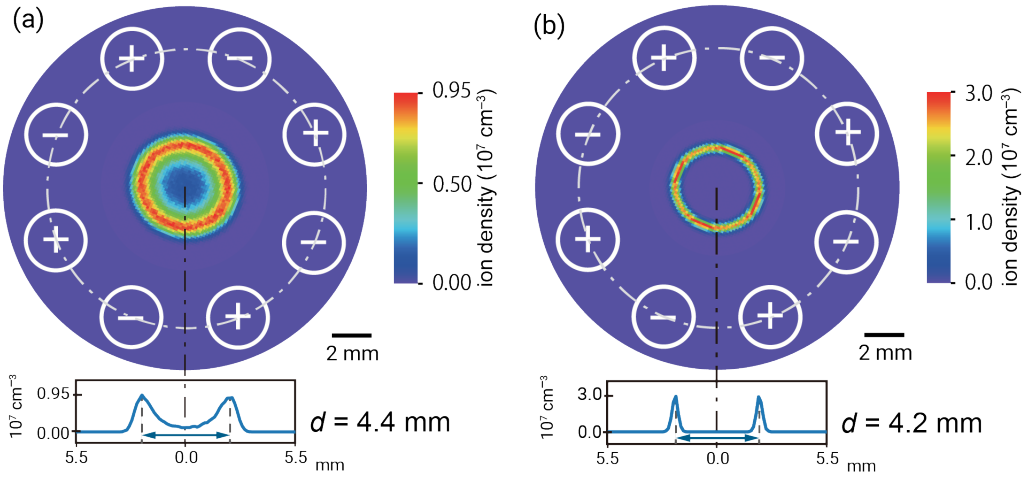

Figure 3-6. 2D histograms of ion distributions in the octopole trap, where the number of trapped ions was reduced to 5.5×10^7, i.e., one-tenth of Figure 3-4. (a) Simulation for the buffer He temperature at 300 K, which shows an effect of the number of ions in the trap by comparing with Figure 3-4. (b) Simulation for the buffer He temperature lowered down to 10 K. The lower panels show ion-density profiles across the center of the trap.

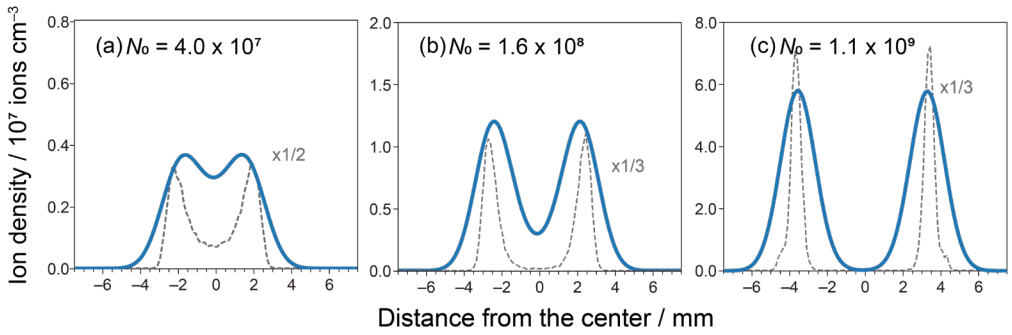

Figure 3-7. Radial ion-distribution profiles across the center of the trap calculated at T = 300 K for different amounts, N_0, of ions stored: (a), (b) and (c) are for N_0 = 4.0×10^7, 1.6×10^8, and 1.6×10^9 ions, respectively. The dashed curves show ion-density profiles as calculated, which are reduced in ordinate by a factor of 1/2 or 1/3. The solid curves, which should be compared with the previous experiment [29], represent ion-density profiles after convolution with a Gaussian function of 2-mm FWHM for taking into account the spot size of the probe laser beam employed in the experiment.

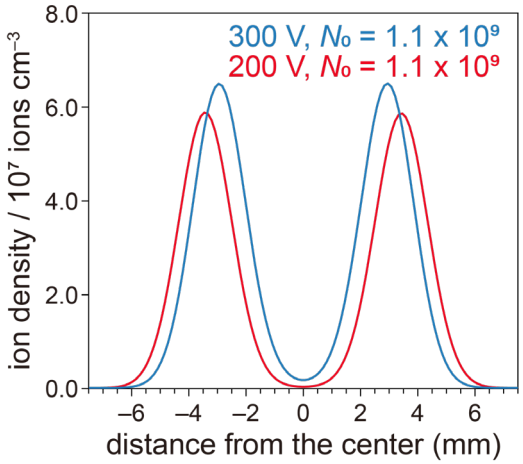

Figure 3-8. Radial ion-distribution profiles calculated at T = 300 K for different rf amplitudes: 200 and 300 V. The profiles are after convolution with a Gaussian-type laser beam spot with 2-mm FWHM. The amount of ions in the trap is1.1×10^9, representing nearly at the space charge limit.

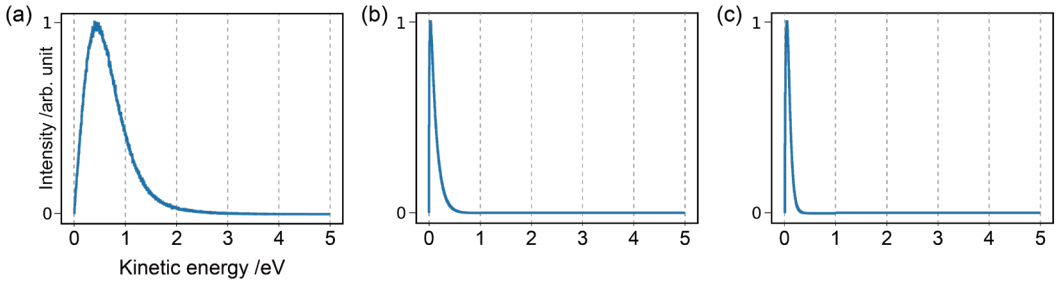

Figure 3-9. Kinetic energy distributions under several conditions.

(a) Buffer-gas temperature: 300 K, ion loading: 5.5×10^8 ions (almost space charge limit). The mean kinetic-energy is 0.7 eV, corresponding to translational temperature about 8,000 K.

(b) Buffer-gas temperature: 300 K, ion loading: 5.5×10^7 ions. The mean kinetic-energy is 0.12 eV, corresponding to translational temperature about 1,400 K.

(c) Buffer-gas temperature: 80 K, ion loading: 5.5×10^7 ions. The mean kinetic-energy is 0.08 eV, corresponding to translational temperature about 900 K.

Quadrupole ion trap: an effect of the electrode structure

We extended the present simulation further to a linear quadrupole ion trap. The trap was assumed to contain 1.3×10^8 ions of Ag_2^+ at 300 K by referring to a previous experiment [29]. Figure 3-10(a) shows a result of simulation for an ordinary linear quadrupole ion trap with four pole electrodes. The stored ions were found to be concentrated around the center of the trap as reported by several experimental studies [10,11]. The radial dependence of the effective potential, Φ, of a quadrupole ion trap is $\Phi \sim r^2$, which is steeper than higher-order multipole traps: $\Phi \sim r^{2n-2}$ for a $2n$-pole trap [3]. A quadrupole ion trap is the only one that can locate ions around the center of the trap even in the presence of space charge. This ion distribution concentrated at the central axis of the trap is advantageous in laser spectroscopy because a laser beam easily overlaps with the ion cloud to create a large interaction volume. Instead, the total amount of ions that can be stored in a quadrupole trap may be less than multipole traps due to the smaller volume of the ion cloud.

A lower-order multipole can generally be arranged by modifying higher-order ones [29,46]. For example, a quadrupole-like equipotential surface is created by the eight electrodes of an octopole by wiring neighboring two poles together to form four pairs of electrodes. Such a quasi-quadrupole trap has been shown to work as well for locating ions at the center of the trap [29] although the structure of the pole electrodes is very different from that of an ordinary quadrupole. Ideally, the pole electrodes should have a hyperbolic surface. But, for practical reasons, they are often substituted with cylindrical ones that approximate well the hyperbolic case [27], as we adopted as well in Figure 3-10(a). However, the electrodes of the quasi-quadrupole is different from the cylindrical one so much that we would expect a change in the ion distribution.

In this context, we performed simulation also on the quasi-quadrupole ion trap under the same conditions of the total amount of ions and the temperature. Figure 3-10(b) shows the result. The ion density exhibits a clear dip at the center, which does not appear in an ordinary quadrupole (Figure 3-10(a)) Distortions of the quadrupole field are usually discussed in terms of the multipole expansion of the effective potential. For an ideal quadrupole trap consisting of hyperbolic-shaped pole electrodes, the potential is expressed only by the quadrupole term. As for a quadrupole trap consisting of cylindrical poles, the higher-order terms are minimized by setting the ratio, r_{pole}/r_0 to be 1.145 as employed for the simulation of Figure 3-10(a), where r_{pole} and r_0 are the radius of the pole electrode and the inscribed radius of the trap, respectively; the potential thus approximates an ideal one [47]. In contrast to these ideal or near-ideal cases, the present quasi-quadrupole trap is expected to have significant contributions of higher-order terms. The dip of the ion density at the center of the trap observed in Figure 3-10(b) must be due to these higher-order multipole fields. The present simulation thus revealed an effect of the electrode structure on the ion distribution in the trap.

The result of simulation in Figure 3-10(b) is to be compared with an experimental result reported in Ref. [29]. The simulation reproduced the experiment reasonably well in that the ions are concentrated at the center of the trap within about 2 mm in diameter, except that the dip was not discernible in the experiment. The reason for the absence of the dip is the finite size (about 2 mm in diameter) of the probe laser, which smears out the dip. As was performed to obtain Figure 3-5(a) from Figure 3-4, Figure 3-10(b) reproduced the experimental result satisfactorily after convolution with a Gaussian profile representing a laser beam.

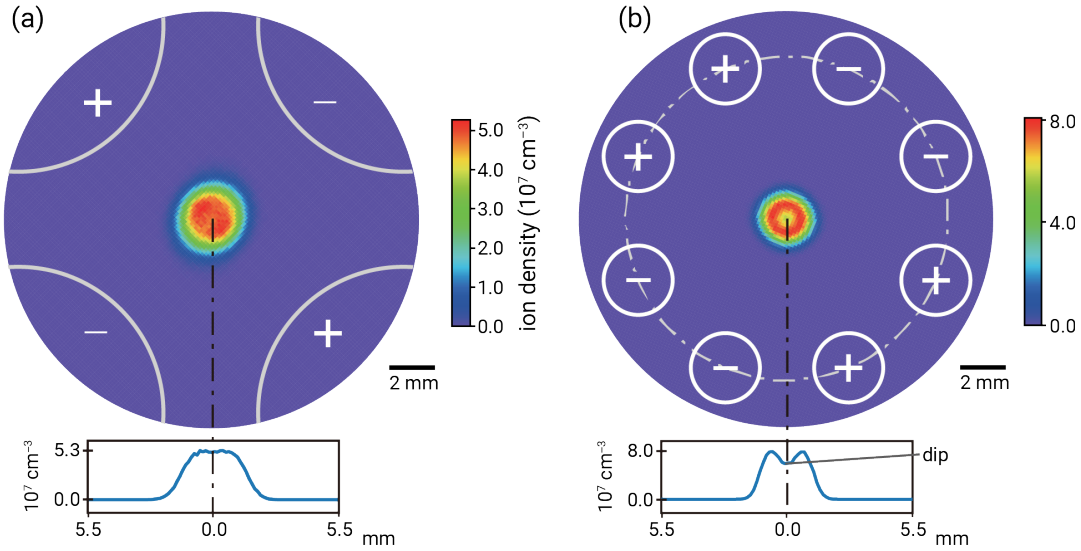

Figure 3-10. Simulation of ion distributions in linear quadrupole traps with different electrode structures. 1.3×10^8 ions of Ag_2^+ are trapped at T = 300 K. (a) An ordinary linear quadrupole trap, where r_{pole}/r_0 was set to 1.145. (b) A quasi-quadrupole trap, where the neighboring poles were wired pairwise to form four pairs of electrodes.

3-4. Summary

We performed ion-trajectory simulations for linear octopole and quadrupole rf ion traps to characterize the ion cloud formed in the trap by employing SIMION. Considering the effects of space charge and buffer-gas thermalization, we were able to reproduce ion-distribution profiles quantitatively that have been reported by experiment. The simulation was extended to investigation of ion-density profiles in several different conditions by varying the total amount of ions stored in the trap, the buffer-gas temperature and the structure of the pole electrodes. In an octopole trap, the ion cloud showed a ring profile, of which diameter was larger for a larger amount of ions due to more significant space charge. When the buffer-gas was cooled from 300 K to 10 K, the thickness of the ion ring was found to become significantly thinner. In a quadrupole trap, on the other hand, ions were distributed almost uniformly at the center of the trap. Note that, when an octopole is converted to a quasi-quadrupole, higher-order multipole fields might modify the uniform distribution, causing an ion-density dip at the center of the trap. As demonstrated by the present simulation study, SIMION would provide a reliable tool for quantitative analysis of multipole rf ion traps.

References

1. W. Paul, *Rev. Mod. Phys.* **62**, 531 (1990). doi: 10.1103/RevModPhys.62.531
2. D. Gerlich, *Adv. Chem. Phys.* **92**, 1 (1992). doi: 10.1002/9780470141397.ch1
3. S. W. Bustamente, M. Okumura, D. Gerlich, H. S. Kwok, L. R. Carlson, and Y. T. Lee, *J. Chem. Phys.* **86**, 508 (1987). doi: 10.1063/1.452302
4. K. R. Asmis, M. Brümmer, C. Kaposta, G. Santambrogio, G. von Helden, G. Meijer, K. Rademann, and L. Wöste, *Phys. Chem. Chem. Phys.* **4**, 1101 (2002). doi: 10.1039/b111056j
5. O. Asvany, P. Kumar, B. Redlich, I. Hegemann, S. Schlemmer, and D. Marx, *Science* **309**, 1219 (2005). doi: 10.1126/science.1113729
6. A. Kamariotis, O. V. Boyarkin, S. R. Mercier, R. D. Beck, M. F. Bush, E. R. Williams, and T. R. Rizzo, *J. Am. Chem. Soc.* **128**, 905 (2006). doi: 10.1021/ja056079v
7. S. Trippel, J. Mikosch, R. Berhane, R. Otto, M. Weidemüller, and R. Wester, *Phys. Rev. Lett.* **97**, 193003 (2006). doi: 10.1103/PhysRevLett.97.193003
8. A. Terasaki, T. Majima, and T. Kondow, *J. Chem. Phys.* **127**, 231101 (2007). doi: 10.1063/1.2822022
10. K. Hirsch, J. T. Lau, P. Klar, A. Langenberg, J. Probst, J. Rittmann, M. Vogel, V. Zamudio-Bayer, T. Möller, and B. von Issendorff, *J. Phys. B: At. Mol. Opt. Phys.* **42**, 154029 (2009). doi: 10.1088/0953-4075/42/15/154029
11. T. Hayakawa, K. Egashira, M. Arakawa, T. Ito, S. Sarugaku, K. Ando, and A. Terasaki, *J. Phys. B: At. Mol. Opt. Phys.* **49**, 075101 (2016). doi: 10.1088/0953-4075/49/7/075101

12. S. Ishiuchi, H. Wako, D. Kato, and M. Fujii, *J. Mol. Spectrosc.* **332**, 45 (2017). doi: 10.1016/j.jms.2016.10.011

13. S. M. Craig, F. S. Menges, and M. A. Johnson, *J. Mol. Spectrosc.* **332**, 117 (2017). doi: 10.1016/j.jms.2016.11.015

14. B. A. Long, D. J. Rodriguez, C. Y. Lau, M. Schultz, and S. L. Anderson, *J. Phys. Chem. C* **124**, 1704 (2020). doi: 10.1021/acs.jpcc.9b10509

15. S. Tainaka, T. Ujihira, M. Kubo, M. Kida, D. Shimoyama, S. Muramatsu, M. Abe, T. Haino, T. Ebata, F. Misaizu, K. Ohshimo, and Y. Inokuchi, *J. Phys. Chem. A* **124**, 9980 (2020). doi: 10.1021/acs.jpca.0c09068

16. D. Gerlich, *J. Chem. Soc. Faraday Trans.* **89**, 2199 (1993). doi: 10.1039/FT9938902199

17. W. Paul, B. Lücke, S. Schlemmer, and D. Gerlich, *Int. J. Mass. Spectrom.* **149**, 373 (1995). doi: 10.1016/0168-1176(95)04269-Q

18. S. Wolf, G. Sommerer, S. Rutz, E. Schreiber, T. Leisner, L. Wöste, and R. S. Berry, *Phys. Rev. Lett.* **74**, 4177 (1995). doi: 10.1103/PhysRevLett.74.4177

19. L. D. Socaciu, J. Hagen, T. M. Bernhardt, L. Wöste, U. Heiz, H. Häkkinen, and U. Landman, *J. Am. Chem. Soc.* **125**, 10437 (2003). doi: 10.1021/ja027926m

20. J. Mohrbach, S. Dillinger, and G. Niedner-Schatteburg, *J. Phys. Chem. C* **121**, 10907 (2017). doi: 10.1021/acs.jpcc.6b12167

21. M. Arakawa, M. Horioka, K. Minamikawa, T. Kawano, and A. Terasaki, *J. Phys. Chem. C* **124**, 26881 (2020). doi: 10.1021/acs.jpcc.0c08890

22. A. Mortensen, E. Nielsen, T. Matthey, and M. Drewsen, *Phys. Rev. Lett.* **96**, 103001 (2006). doi: 10.1103/PhysRevLett.96.103001

23. K. Okada, K. Yasuda, T. Takayanagi, M. Wada, H. A. Schuessler, and S. Ohtani,

Phys. Rev. A - At. Mol. Opt. Phys. **75**, 033409 (2007). doi: 10.1103/PhysRevA.75.033409

24. O. Asvany, F. Bielau, D. Moratschke, J. Krause, and S. Schlemmer, *Rev. Sci. Instrum.* **81**, 076102 (2010). doi: 10.1063/1.3460265

25. K. Geistlinger, M. Fischer, S. Spieler, L. Remmers, F. Duensing, F. Dahlmann, E. Endres, and R. Wester, *Rev. Sci. Instrum.* **92**, 023204 (2021). doi: 10.1063/5.0040866

26. R. Wester, *J. Phys. B.: At. Mol. Opt. Phys.* **42**,154001 (2009). doi: 10.1088/0953-4075/42/15/154001

27. S. Guan and A. G. Marshall, *J. Am. Soc. Mass Spectrom.* **5**, 64 (1994). doi: 10.1016/1044-0305(94)85038-0

28. M. W. van Mourik, P. Hrmo, L. Gerster, B. Wilhelm, R. Blatt, P. Schindler, and T. Monz, *Phys. Rev. A* **105**, 033101 (2022). doi: 10.1103/PhysRevA.105.033101

29. T. Majima, G. Santambrogio, C. Bartels, A. Terasaki, T. Kondow, J. Meinen, and T. Leisner, *Phys. Rev. A* **85**, 053414 (2012). doi: 10.1103/PhysRevA.85.053414

30. R. Otto, P. Hlavenka, S. Trippel, J. Mikosch, K. Singer, M. Weidemüller, and R. Wester, *J. Phys. B.: At. Mol. Opt. Phys.* **42**, 154007 (2009). doi: 10.1088/0953-4075/42/15/154007

31. C. Champenois, *J. Phys. B.: At. Mol. Opt. Phys.* **42**, 154002 (2009). doi: 10.1088/0953-4075/42/15/154002

32. J. Walz, I. Siemers, M. Schubert, W. Neuhauser, R. Blatt, and E. Teloy, *Phys. Rev. A* **50**, 4122 (1994). doi: 10.1103/PhysRevA.50.4122

33. J. D. Prestage, R. L. Tioelker, and L. Maleki, *Proceedings of the 2000 IEEE/EIA International Frequency Control Symposium and Exhibition* 706 (2000).

doi: 10.1109/FREQ.2000.887441

34. I. Siemers, R. Blatt, Th. Sauter, and W. Neuhauser, *Phys. Rev. A* **38**, 5121 (1988). doi: 10.1103/PhysRevA.38.5121

35. P. H. Hemberger, N. S. Nogar, J. D.Williams, R. G. Cooks, and J. E. P. Syka, *Chem. Phys. Lett.* **191**, 405 (1992). doi: 10.1016/0009-2614(92)85400-5

36. C. D. Cleven, R. G. Cooks, A. W. Garrett, N. S. Nogar, and P. H. Hemberger, *J. Phys. Chem.* **100**, 40 (1996). doi: 10.1021/jp951667o

37. D. J. Manura and D. A. Dahl, *SIMION 3D Version 8.0, Scientific Instrument Services, Inc.* (2008).

38. H. G. Dehmelt, *Adv. At. Mol. Phys.* **3**, 53 (1968). doi: 10.1016/S0065-2199(08)60170-0

39. A. Terasaki, T. Majima, C. Kasai, and T. Kondow, *Eur. Phys. J. D* **52**, 43 (2009). doi: 10.1140/epjd/e2008-00274-0

40. P. Weis, T. Bierweiler, S. Gilb, and M. M. Kappes, *Chem. Phys. Lett.* **355**, 355 (2002). doi: 10.1016/S0009-2614(02)00277-4

41. D. Manura (2007). Scientific Instrument Services, Inc. Licensed under the terms of SIMION 8.0.

42. SIMION Charge Repulsion, https://simion.com/info/charge_repulsion.html, accessed December 2022.

43. SIMION Collison Model HS1, https://simion.com/info/collision_model_hs1.html, accessed January 2023.

44. O. Asvany and S. Schlemmer, *Int. J. Mass Spectrom.* **279**, 147 (2009). doi: 10.1016/j.ijms.2008.10.022

45. K. Egashira, C. Bartels, T. Kondow, and A. Terasaki, *Eur. Phys. J. D* **63**, 183

(2011). doi: 10.1140/epjd/e2011-10525-6

46. M. Niranjan, A. Prakash, and S. A. Rangwala, *Atoms* **9**, 38 (2021). doi: 10.3390/atoms9030038

47. D. J. Douglas and N. V. Konenkov, *Rapid Commun. Mass Spectrom.* **16**, 1425 (2002). doi: 10.1002/rcm.735

Part 2

Characterization of water droplets in a vacuum

Chapter 4. Evaporative cooling and homogeneous freezing of water droplets

4-1. Introduction

Observation of evaporation and freezing processes of water droplets in a vacuum is expected to reveal novel phenomena that are hidden in the atmosphere. Free evaporation induces rapid evaporative cooling as the evaporating water molecules carry heat away from the droplet without condensation back to the liquid phase. Such fast evaporative cooling offers a possibility to investigate supercooled water. The temperature of such water droplets in a vacuum was reported to be 250 K for droplet size of ~10 μm [1] and 230 K for those of 12 μm [2] via Raman thermometry. One conventional way of temperature estimation is based on the Knudsen kinetic model [1, 3-5]. Water can exist in the liquid state at temperatures far below its normal melting point. The freezing process of water is either heterogeneous or homogeneous. As the small sample size (about 50 pL) of a micro-meter droplet suppresses heterogeneous nucleation sites, micrometer-sized water droplets in a vacuum can be useful to investigate supercooled water and homogeneous ice nucleation. Formation of homogeneous frozen nuclei is not limited to laboratory measurements but also prevails for supercooled water observed in cirrus clouds at altitude above 1.6 km, where the lack of ice nuclei is expected [6, 7]. Supercooled water at –38 to –35°C in clouds observed by in situ measurements is consistent with the lowest temperature of 10 to 100-μm water droplets supercooled in laboratory experiments [8].

The freezing process of supercooled water droplets starts from a dendritic growth phase both for homogeneous [9] and for heterogeneous ice nucleation [10, 11]. After nucleation, ice grows until the latent heat released by crystallization raises the droplet temperature to the melting point. During the early stage of freezing, water droplets moving at a constant velocity were observed to be deflected spontaneously in a vacuum [5]. This motion is discussed to be caused by the release of the latent heat, which induces localized evaporation [9]. The structure of supercooled water near the temperature of homogeneous ice nucleation differs from that of water at room temperature, suggesting a tetrahedral ordering as observed by femtosecond X-ray laser [4]. Heterogeneous freezing of supercooled water droplets at an atmospheric pressure was studied by laboratory measurements, where fragmentations of different droplet sizes were reported [11, 12].

Due to the inaccessibility to the supercooled regime, the homogeneous ice nucleation rate still remains as curious topics of ongoing experimental research. The ice nucleation rate is expected to increase as the temperature decreases. Most of the experiments of homogeneous ice nucleation use micro-meter droplets to reach between ~235 and ~240 K [13-19]. On the other hand, experiments with nano-meter droplets offer even higher nucleation rates to reach the range between ~195 and 225 K [18-21]. In the intermediate temperatures, micrometer droplets in a vacuum serve as one approach; e.g., Laksmono et al. reported the volume-based homogeneous ice nucleation rate (J_v) from ~227 to 232 K. Also, Hagen et al.[22] reported J_v in the same temperature range, although the values exhibit discrepancies beyond the measurement errors.

In this study, 40-μm water droplets were introduced into vacuum to observe evaporation and homogeneous freezing processes. We measured the droplet size as a

function of time after injection into vacuum via observing whispering gallery modes (WGMs) of cavity enhanced Raman scattering on a single-laser-shot basis. The evaporative cooling rate calculated from the time evolution of the droplet diameter can be compared with that obtain computationally by the Knudsen theory. Also, a CW laser was used to probe the individual droplet at various distances from the nozzle exit, hence varying the droplet temperature. An image of scattered light at an right angle allowed us to observe formation of ice. Freezing time of each droplet gives us a homogeneous ice nucleation rate between 232–235 K that fills the temperature gap between the data of Hagen et al. [22], Laksmono et al. [23], and micro-droplets measured at various ambient pressures.

4-2. Setup for micro-droplet generation in a vacuum

The procedure for generating micro-meter sized droplets in a vacuum is described below. We used distilled water (Wako Pure Chemical Industries, Ltd) as a sample of water. The droplet generation setup is shown in Figure 4-1, which improved the previous one described elsewhere [5, 24]. We have applied a trigger voltage to a piezo driven dispenser head (MD-K-130, microdrop Technologies GmbH) with a controller card (uDropC-170) for injecting a droplet. For orifices of less than 30 μm, clogging is the most serious issue that could disturb the droplet generation. A polyvinylidene difluoride (PVDF) membrane filter (5 μm pore size) was applied for purification and particle removal from the sample water to avoid clogging the nozzle. We believe that, after the filtration, water is free from particles that might act as heterogeneous nuclei. If some of the droplets had contained some particulates, these droplets would have shown separate nucleation statistics within the ensemble of the other clean droplets. The

dispenser head uses the principle of the ink jet printing technology. The core of the dispenser head consists of a glass capillary with an inner diameter of 30 μm and a tubular piezo actuator surrounding the capillary. The droplet size was adjustable in the range of 35–50 μm in diameter (corresponding to 22 to 65 pL) by adjusting the duration and amplitude of the pulsed voltage applied to the piezo actuator. The dispenser head was sealed by an O-ring upon installation in the vacuum chamber.

There are experimental difficulties in introducing a volatile liquid into a vacuum. The procedure is somewhat complicated because the dispenser head is not intended for use in a vacuum. The dispenser head, liquid reservoir, and connecting tube are cooled to 273–277 K by ice. This operation lowers the saturated vapor pressure of water by an order of magnitude down to 6×10^2 Pa and raises the viscosity by a factor of two compared with that at room temperature. As a result, it stabilizes generation of water droplets in a vacuum, as described below. The sample water is deaerated by evacuating the reservoir below 10^2 Pa prior to droplet generation because bubbles of dissolved gases inside the glass capillary in the dispenser head hinder stable and reproducible droplet generation. For ejecting water droplets, the glass capillary must be filled to its tip with water. After evacuating the vacuum chamber and the sample reservoir to 15 kPa, the needle valve (SS-1RS4, Swagelok Co.) was closed to stop evacuation of the sample reservoir and to keep evacuating only the vacuum chamber (13 kPa) so that the deaerated water was transferred to the nozzle through a perfluoroalkoxy (PFA) tube. This operation must be performed at a pressure higher than the saturated vapor pressure of water (3 kPa at room temperature) to prevent the water from freezing. The needle valve for evacuation of the liquid reservoir was opened immediately after the water spills out from the nozzle.

The water that overflowed at the tip of the nozzle was pulled back by siphoning, i.e., by adjusting the height of the sample reservoir lower than the nozzle.

After confirming no more water at the tip of the nozzle, we started droplet generation by adjusting the timing, amplitude, and duration of the pulsed voltage applied to the piezo actuator. The pressure of the chamber was lowered slowly to the pump's ultimate pressure of 1 Pa over 1 hour by slightly opening the diaphragm valve (speedivalve, Edwards Ltd.) just above the pump (NeoDry15E, Kashiyama Industries, Ltd.) while the droplet nozzle was operated continuously. Also, the liquid reservoir pressure was slowly reduced close to the saturated vapor pressure of water by adjusting the pressure modulation needle valve and holding it slightly open. One hour of depressurization was so slow that formation of water droplets was not interrupted because the conductance difference between the chamber and the reservoir was negligible. As a result, micrometer-sized water droplets can be produced on demand at 1 Pa for up to 2 hours, allowing us to perform water-droplet spectroscopy on a one-shot basis.

There are some other methods for injecting droplets into a vacuum. Water droplets in a vacuum are often produced from a laminar jet [25]. In the laminar flow, a liquid is ejected as a continuous cylindrical filament before it eventually breaks up spontaneously at a certain critical distance downstream of the aperture into a directional stream of spherical droplets. The jet instability responsible for droplet formation was first described by Rayleigh [26], which is now named after him. The Rayleigh instability can be triggered by an excitation applied externally at a frequency close to the intrinsic Rayleigh frequency [27, 28]. An approach to create water droplets of 10 μm or less, while avoiding clogging, has been demonstrated for water jets by Deponte et al. [29], which is known as a so-called gas dynamic virtual nozzle (GDVN). Compared with these

methods, the present method using a piezo-driven dispenser head can reduce the rate of droplet generation down to 5 Hz, which allows us to interrogate a single droplet.

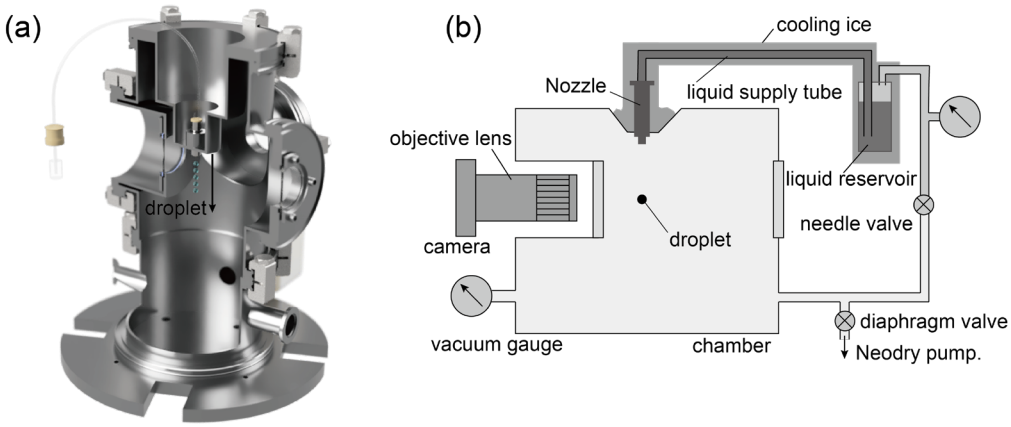

Figure 4-1. (a) Rendered view of droplet generation system for droplet generation in a vacuum. (b) Schematic view of the setup.

4-3. Size measurement from whispering gallery modes

Theory of whispering gallery mode resonance

In this principle, the diameter of a sphere is measured based on an analysis of the wavelengths of whispering gallery modes (WGMs). The term comes from L. Rayleigh's discovery that a speaker, close to the base of the dome, simply whispering to the wall could be heard clearly by listers far away on the opposite side. The relationship between the WGM wavelengths and the diameter of the sphere can be obtained by solving the following dispersion equation [30, 31]. The droplet is assumed to be a perfect sphere.

$$\frac{1}{j_l(\rho_1)}\frac{\partial[\rho_1 j_l(\rho_1)]}{\partial\rho_1} = \frac{\mathrm{a}}{h_l^{(1)}(\rho_2)}\frac{\partial\left[\rho_2 h_l^{(1)}(\rho_2)\right]}{\partial\rho_2} \quad (1)$$

Here, $j_l(\rho_1)$ is the spherical Bessel function, $h_l^{(1)}(\rho_2)$ is the spherical Hankel function, subscript l is the angular mode number, and $\rho_{1,2} = \pi d n_{1,2}/\lambda_0$ is the size parameter, where n is the refractive index (the subscripts 1 and 2 denote a sphere surrounded by vacuum and air, respectively), λ_0 is the wavelength of light in a vacuum, and d is the diameter of the sphere. a is the polarization dependent factor that is μ_2/μ_1 for TE modes and $\mu_2 {n_1}^2/\mu_1 {n_2}^2$ for TM modes.

Simulation of Whispering Gallery Mode

In 1908, Gustav Mie developed a rigorous method to calculate the intensity of light scattered by uniform spheres. Although Mie's solution was precise, it involved a considerable number of calculations for large spheres and was rarely used until the 1980s when supercomputers became available for scientific research. The rapid advances in the computer power over the last few years allow Mie scattering calculations even on standard personal computers. The software MiePlot [32] offers mathematical models for scattering of light by a homogeneous sphere.

In this study, the author simulated scattering intensity from a spherical particle upon illumination of a narrow beam of light. Figure 4-2 shows the result of simulation of Mie scattering from a 40-μm water droplet. The profile of illumination is assumed to be a Gaussian beam. MiePlot's calculations for Gaussian beams are based on the Mie theory algorithms [33, 34]. The polarization of incident light was assumed to be parallel to the surface of a droplet. The water droplet was assumed to be surrounded by a vacuum. The illumination beam with a 20-μm half width was positioned at the edge of the water droplet. The refractive index of water is cited from IAPWS [35]. As shown in Figure 4-2, scattering intensity is observed only for the TE mode, which originates from the direction of the incident light and the surface of the water droplet. The resonances at 640.7 and 642.1 nm are known as whispering-gallery modes (WGMs) or morphology-dependent resonances (MDRs). These resonances seem to be almost independent of the scattering angle.

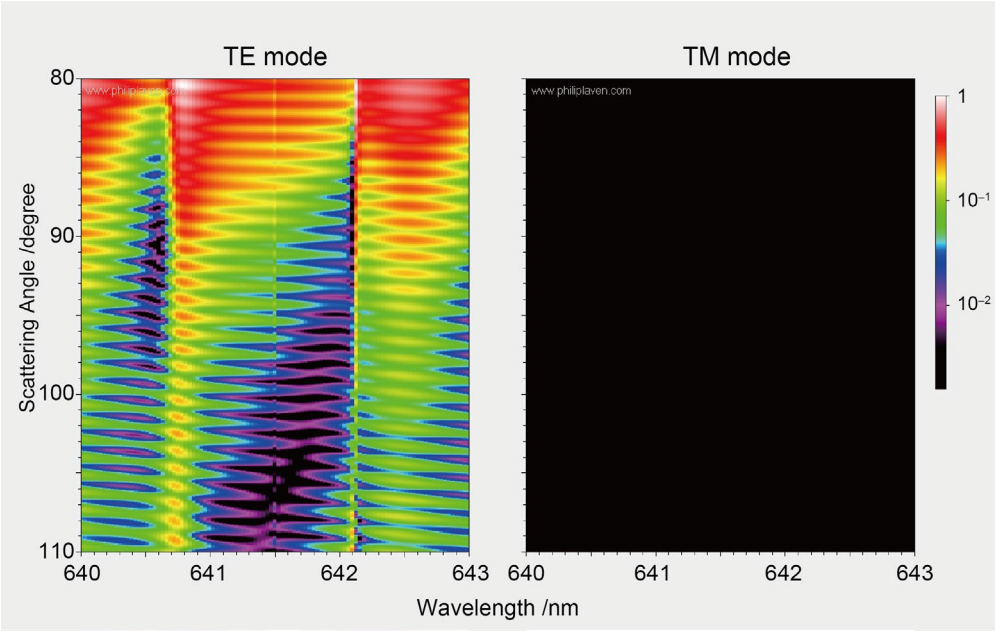

Figure 4-2. Intensity of scattered light as a function of the scattering angle and the wavelength of incident light. (a) The polarization is parallel to the surface of a droplet. (b) The polarization is perpendicular to the surface of a droplet.

To estimate the diameter from the dispersion equation (1), firstly, WGM wavelengths are measured. Secondly, it is necessary to determine the angular mode numbers *l* and the polarization for the measured WGM wavelengths to identify the radial mode number. By solving equation (1) numerically, the relationship between resonance wavelengths and the sphere diameter can be obtained. Figure 4-3 shows the resonance wavelengths of 40-μm water droplets. The refractive index is cited from Duft et al. [36]. The temperature is set to room temperature (300 K). Wavelength dispersion of the refractive index is taken into account [37]. The wavelength-dependent refractive index will be discussed in detail in the next chapter. Several combinations of resonance wavelengths and angular mode numbers are obtained. The resonance wavelengths connected by a dotted line show a series of angular modes belonging to the same radial mode. In particular, the series of the maximum angular mode numbers corresponds to a radial mode (n = 1) with electric-field strength localized at the outermost edge of the sphere.

The concept of fitting is designed so that parameters describing the sphere are explored until the difference between the observed and calculated modes is minimized. It is more convenient to determine a free spectral range (FSR) between each WGM wavelength experimentally; determination of FSR is more accurate and less likely suffer from adjustment problems than an absolute WGM wavelength. Therefore, the droplet size was determined from FSR up to 0.1 μm, while absolute WGM wavelengths were used for droplets less than 10 nm in diameter. FSR is plotted for the radial mode of n = 1 as a function of the droplet diameter in Figure 4-4. The FSRs are obtained in the range of 620 – 670 nm, where the OH Raman band of water appears. The FSR increases as the droplet size reduces.

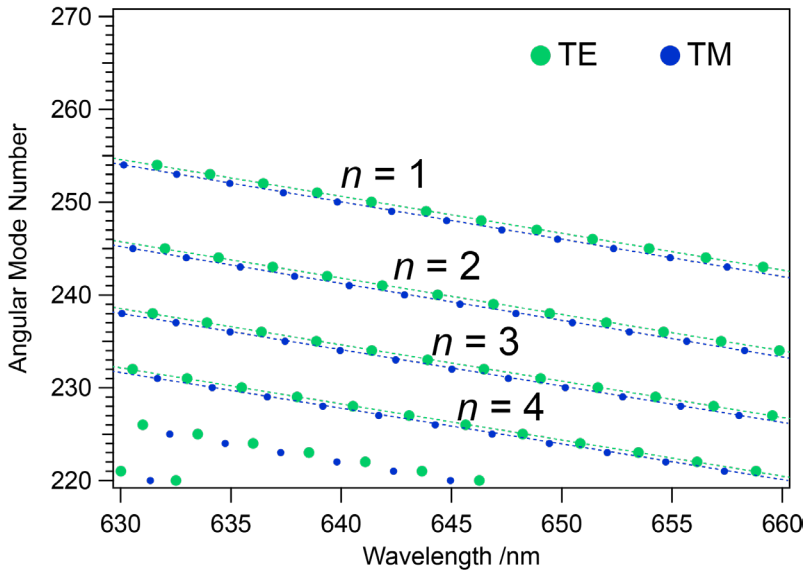

Figure 4-3. Angular mode number as a function of the wavelength of 40 μm droplet. (TE) The polarization is parallel to the surface of a droplet. (TM) The polarization is perpendicular to the surface of a droplet.

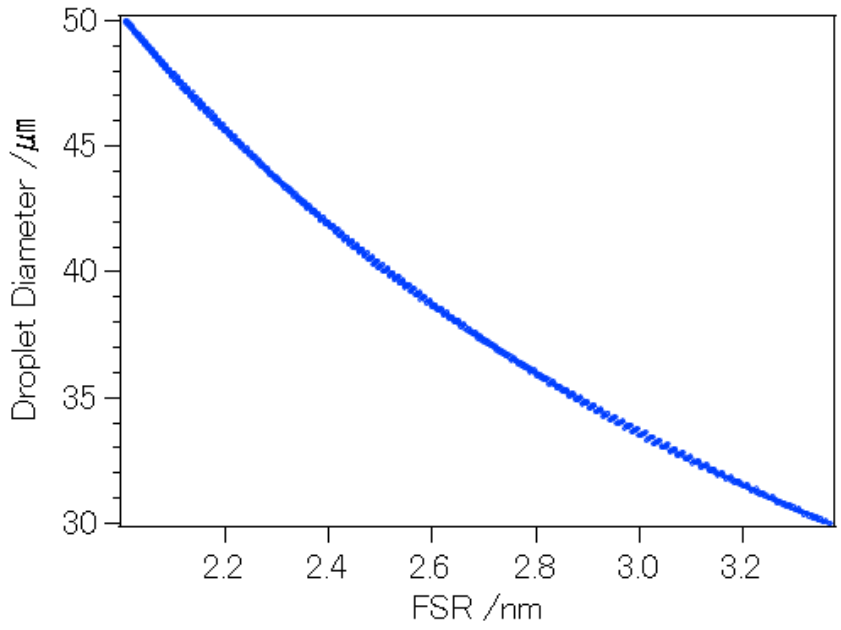

Figure 4-4. Droplet diameter as a function of the free spectral range of WGM resonances: the radial mode is n = 1 with the TM polarization. The temperature dependence and dispersion of the refractive index are taken into account.

Refractive index of supercooled water

The refractive index of water is the only physical constant taken into account in the estimation of the droplet size from the dispersion equation (1). The refractive index of water is 1.33284 at room temperature (283 K) at the wavelength of 632.8 nm; the refractive index above 0° C has been determined with an accuracy better than 1×10^{-5}. Such high-precision measurements were carried out by employing various interferometers. However, there are only a few reports about the refractive index of supercooled water [38-41]. The lower limit of the temperature is –15°C for refractive index measurement using interferometers [42]. The reasons for the difficulty is speculated as follows. 1. Thermal expansion/shrinking of the water container also causes a change in the optical path length, which cannot be discriminated from the temperature-dependent change in the refractive index. 2. To reach the supercooled temperature, small-volume water cells are needed. However, such a small water cell lowers the resolution of measurement [42].

Determination of the refractive index of supercooled water (< –15°C) can be achieved by water droplets. T. Leisner and co-workers presented a novel method for determination of the refractive index of a single droplet by light scattering in the region of the first and second order rainbow [36]. By cooling 90-μm water droplets, the refractive index of water was extended to a previously inaccessible region down to 237 K. The lowest temperature of this measurement is limited by the homogeneous ice nucleation rate. It has been reported that the smaller the droplet size, the lower the freezing temperature [5]. The refractive index of water has been reported in the range between 237 and 365 K [36, 38, 42, 43]. We performed fitting the refractive-index data using a forth order polynomial:

$$n(T) = a_0 + a_1 T + a_2 T^2 + a_3 T^3 + a_4 T^4 \,, \qquad (2)$$

where $a_0 = -1.5064$, $a_1 = 0.035718$, $a_2 = -0.00016791$, $a_3 = 3.5054 \times 10^{-7}$, and $a_4 = -2.7536 \times 10^{-10}$.

Dispersion (wavelength dependence of the refractive index) of supercooled water has not been measured, to the best of our knowledge, because it requires a measurement precision as high as 10^{-6}. In the Raman spectroscopy of water, the peak width (FWHM: full width at half maximum) of the OH-stretching band is only 17 nm when the excitation wavelength is 532 nm. Therefore, the order of dispersion that needs to be taken into account of the Raman peak is as small as 10^{-5}. Although the influence on the precision in the droplet size evaluation is expected to be small, the present study compares the droplet sizes obtained with and without refractive-index dispersion for high accuracy. Figure 4-4 shows the relationship between the droplet diameter and the free spectral range of WGM. Without accounting for dispersion, there was a maximum deviation of ~ 0.50 μm in droplet size with respect to the size estimated with dispersion taken into consideration (Figure 4-5). The dispersion of water was cited from the four-term Sellmeier dispersion formula measured at 297.0 K using a goniometer spectrometer [37]. We couldn't find reports on such dispersion in supercooled water as far as we know. In this study, we performed linear interpolation of Masumura's wavelength dispersion [37] using temperature dependent refractive index at the wavelength, 632.8 nm, of a He-Ne laser [36].

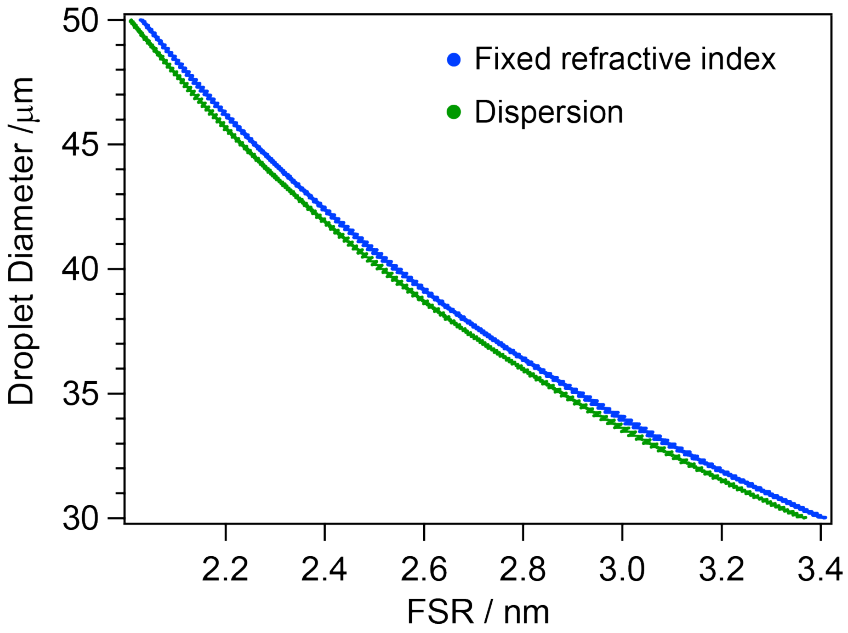

Figure 4-5. Droplet diameter as a function of the free spectral range of WGM resonances: the radial mode $n = 1$ and TM polarization are assumed. Free spectral ranges are calculated from the WGM resonances between 640–670 nm. (green line) the wavelength dispersion was taken into account at 297.0 K. (blue line) the refractive index was fixed at 1.331536 @640 nm, 24°C.

Measurement of WGM resonances in the OH Raman band

The apparatus employed in this study is shown in Figure 4-6. A droplet generator (MD-K-130, micro-drop Technologies GmbH) was vertically mounted on the vacuum chamber. The detail of the droplet generator was mentioned in Sec. 4-2. A gap between the nozzle and the chamber was sealed with an O-ring rubber. The pressure inside the chamber was about 2 Pa by evacuating with a dry pump (NeoDry15E, Kashiyama Industries, Ltd.) at a pumping speed of 250 L/min.

The setup for Raman spectroscopy, including optical devices for excitation and signal acquisition, is also depicted in Figure 4-6. For excitation, a linearly polarized pulsed laser beam at a wavelength of 532.05 nm emitted from second harmonics of a Q-switched Nd:YAG laser (VM-2134UTF ,VM-TIM GmbH) was directed to the droplet edge. The wavelength was measured with a wavemeter (WF6, HighFinesse). The laser power was set to <0.3 mJ/pulse. The spot size at the droplet was adjusted to 30 μm in diameter. A window with anti-reflection coating (Sigmakoki, WBMA-50C05-10-550) was installed to the path of the excitation laser light. For signal acquisition, Raman scattering was collected by a telecentric objective lens (ML×10, Mitsutoyo Corp., NA: 0.21, working distance: 51 mm) that maintains consistent droplet size regardless of focal conditions either in or out of focus. This objective lens combines a long working distance to access the droplet in the chamber and a high NA to collect scattered light. A homemade microscope system was created to combine the objective lens with a camera and a spectrometer (customized YSM-8102-06 series). The pixel size of this camera is 5.86 μm, which gives a depth of field of 40 μm. As for the spectrometer, a fiber optic spectrometer is employed, which will be described in detail in the following paragraphs. Since the slit of the spectrometer has a height of 1,000 μm, an optical fiber with a core diameter of

1,000 μm (P1000-2-UV-VIS, Ocean Insight, Inc.) was employed to maximize the range of light taken in. Rayleigh scattering light was introduced to a C-mount CMOS camera (IMX-249, Sony Corp.) by a long-pass dichroic mirror (DMLP550R, Thorlabs Inc.) The spatial resolution of the image was 0.6 μm/pixel. The leakage of Rayleigh scattering light was filtered by a long pass filter (RSF-25C-532RU, Sigmakoki Corp., OD6@532 nm).

The homemade Raman spectrometer mentioned above has undergone multiple optimizations: (1) adjustment of the laser pulse energy, (2) NA of the objective lens, and (3) S/N and spectral resolution of the spectrometer for acquiring Raman scattering light resonating with water droplets. (1) As the pulse energy of the 532.05 nm excitation laser light increases from 60 to 700 μJ/pulse, the scattering intensity increases proportionally. However, water droplets no longer retain their shape due to laser ablation above 360 μJ/pulse (Figure 4-7). Therefore, the power of excitation laser light was adjusted to be below 180 μJ. (2) The numerical aperture must be high (> 0.15) to perform Raman spectroscopy of ~50 μm water droplets by a single-shot basis. The angular aperture of the lens is approximately twice the NA within the paraxial approximation. At the trial stage of instrumentation, an objective lens (ML ×3, Mitsutoyo Corp., NA: 0.09, working distance 77 mm) was installed to collect scattered light. However, the angular aperture is 5.5 times smaller than that of ML ×10, which is below the detection limit of the spectrometer. (3) The resolution and sensitivity of spectrometers are competing with each other. The best combination of resolution and sensitivity was tested by three spectrometers: USB-2000+ (Ocean Insight, Inc., grating: 200–850 nm, slit: 50 μm), FLAME-S (Ocean Insight, Inc., grating: 200–850 nm, slit: 10 μm), and customized YSM-8102-06 (YIXIST Co., Ltd., grating: 300–830 nm, slit: 5 μm). The former two spectrometers were shown to have a resolution insufficient to distinguish the WGM

resonance peak of a 40-μm water droplet. Therefore, we customized the spectrometer (YSM-8102-06) to obtain higher resolution and sensitivity by increasing the groove density of the grating from 600 to 500 grooves/mm and by reducing the slit width to 5 μm at the same time; the measurement wavelength range was thus reduced to 300–830 nm.

Figure 4-8 shows the WGM resonances observed in the OH stretching Raman band by using the three spectrometers with different resolution. The Raman scattering in a cavity is also called cavity enhanced Raman scattering (CERS). Figure 4-8(a) shows the CERS spectrum with a bandwidth narrower than the typical one reported by J. P. Reid, who also reported the relationship between the CERS and the laser pulse energy [44]. The bandwidth progressively narrows as the pulse energy increases. It should be noted that the gain of the cavity increases with laser fluence until it is saturated above 0.4 GW/cm^2 [44]. The saturation should be avoided because it causes distortions in the profiles of the CERS peaks. In this experiment, the laser fluence was adjusted to a value of 0.2 MW/cm^2. Figure 4-8(b) shows one example of WGM resonances measured by the FLAME-S spectrometer with a moderate resolution. Essentially, the CERS line profiles are symmetrical. In some cases, however, the line profiles appeared asymmetric depending on the droplet size and the illumination geometry. It was found that spectrometers with a higher resolution can discriminate lower intensity peaks of different mode origins as demonstrated in Figure 4-8(c), where the customized YSM-8102-06 spectrometer shows a resolution and a *S/N* ratio sufficiently high to measure WGM resonances of a 40-μm droplet.

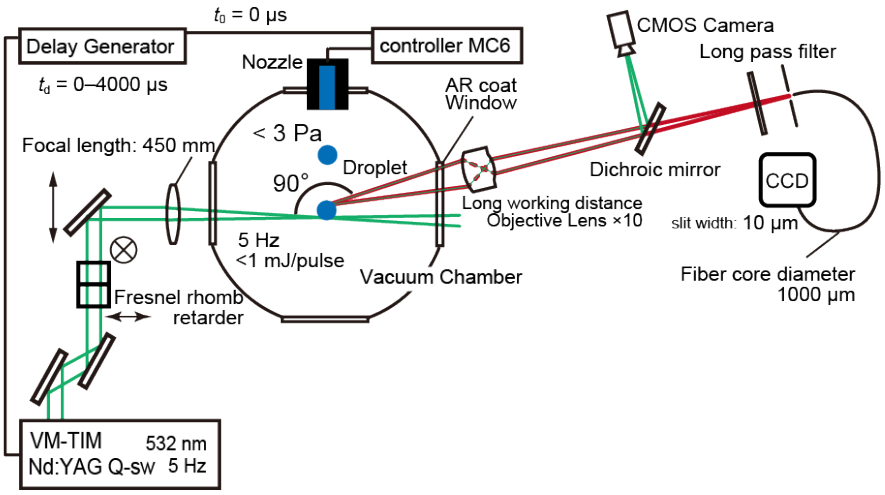

Figure 4-6. A schematic of the experimental configuration for the Raman Whispering Gallery Mode measurement.

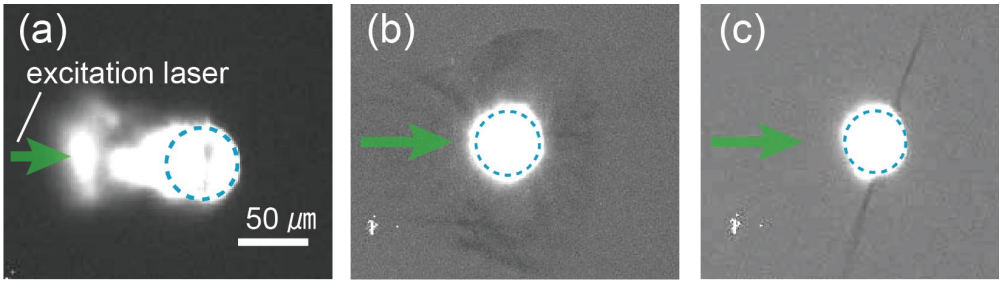

Figure 4-7. Bright field images of droplets upon excitation by an 0.7 mJ pulse at 532 nm from the left-hand side as shown by arrows. The bright area are Raman scattering light, whereas the dark area are fragments of water droplets destructed by laser ablation. The expansion of water was observed in all directions depending on the experimental conditions; for example, backward (a), in all angles (b), and in directions perpendicular to the laser beam (c).

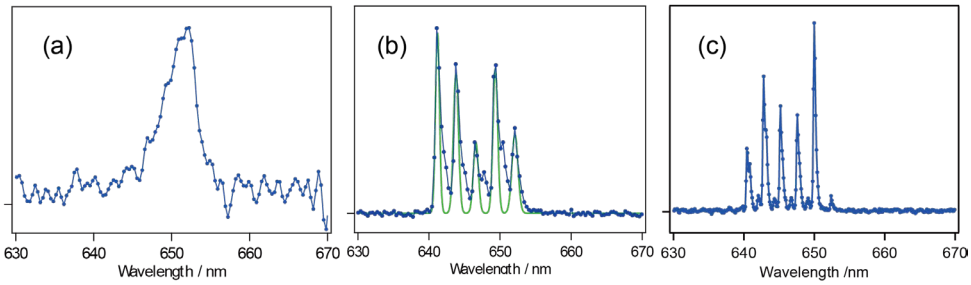

Figure 4-8. Examples of WGM resonances measured by three spectrometers. (a) USB-2000+ (the lowest resolution): Multiple WGM resonance peaks are observed as an unresolved single peak due to low resolution. (b) FLAME-S (moderate resolution): A green solid line is a fitting curve with five Gaussian profiles. (c) customized YSM-8102-06 (the highest resolution): All the spectral lines are separately observed resolving each WGM resonance.

Polarization dependence of Raman whispering gallery modes

When a water droplet of ~40 μm in diameter was illuminated with a 532-nm laser beam near its edge, bright spots were observed as can be seen in Figure 4-9. The intensity profile of Figure 4-9(a) is observed in most of the case, which indicates light propagating along the equator of the sphere (x–y plane). Schematic views of excitation (green line) and scattering light (red line) of WGMs are shown in Figure 4-10, following the ray optics.

The analysis of polarization properties of Raman WGMs is shown in Figure 4-11. In the experiment, polarization of the excitation laser light at 532.0 nm was adjusted by a double Fresnel rhomb retarder, where two orthogonal polarizations were examined. The Raman WGMs were filtered by a polarizer. Figures 4-11(a) and (c) were assigned to Transverse Electric (TE) and Transverse Magnetic (TM) modes, respectively, both for excitation and for detection of Raman WGMs. Much less intensity (< 1/3) was detected for the scattering light in the polarization orthogonal to that of excitation (Figures 4-11 (b) and (d) as well as Figure 4-9(c)), which shows that the Raman WGMs retain the polarization of the incident laser. The band contours of Figures 4-11(a) and (c) suggest that the intensity of each Raman WGM depends on TE/TM modes. The details of the polarization dependence of Raman WGMs are discussed by L. Mitchem et al. [45].

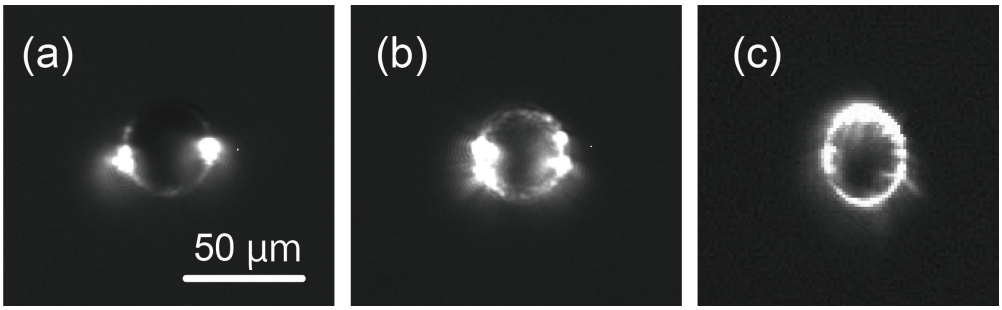

Figure 4-9. Images of Raman whispering gallery modes created in water droplets. An experimental setup is shown in Figure 4-6. A long-pass filter (OD6@532 nm) is inserted between the camera and the dichroic mirror. (a and b) Images frequently observed, which were detected by the scheme of Figure 4-10. (c) An image observed occasionally with an intensity lower than (a and b).

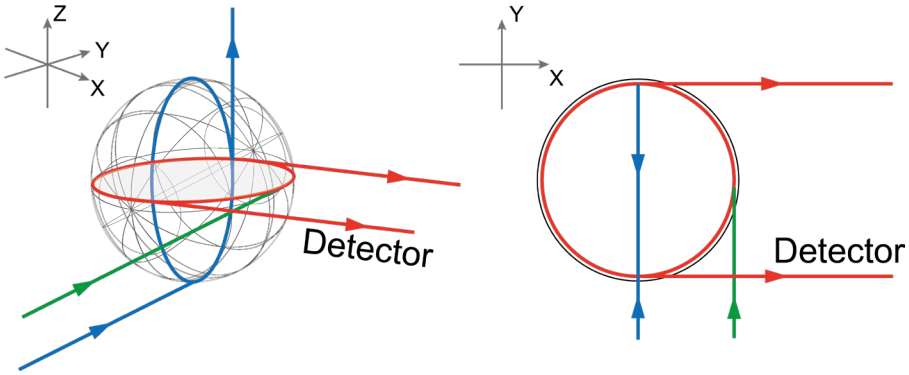

Figure 4-10. Schematic views of WGMs propagating in the equator of the sphere. Green and blue lines show the incident light. The red line indicates the WGMs detectable by the spectrometer in the x-axis direction. Depending on the position of the detector, WGMs are selectively acquired (red line).

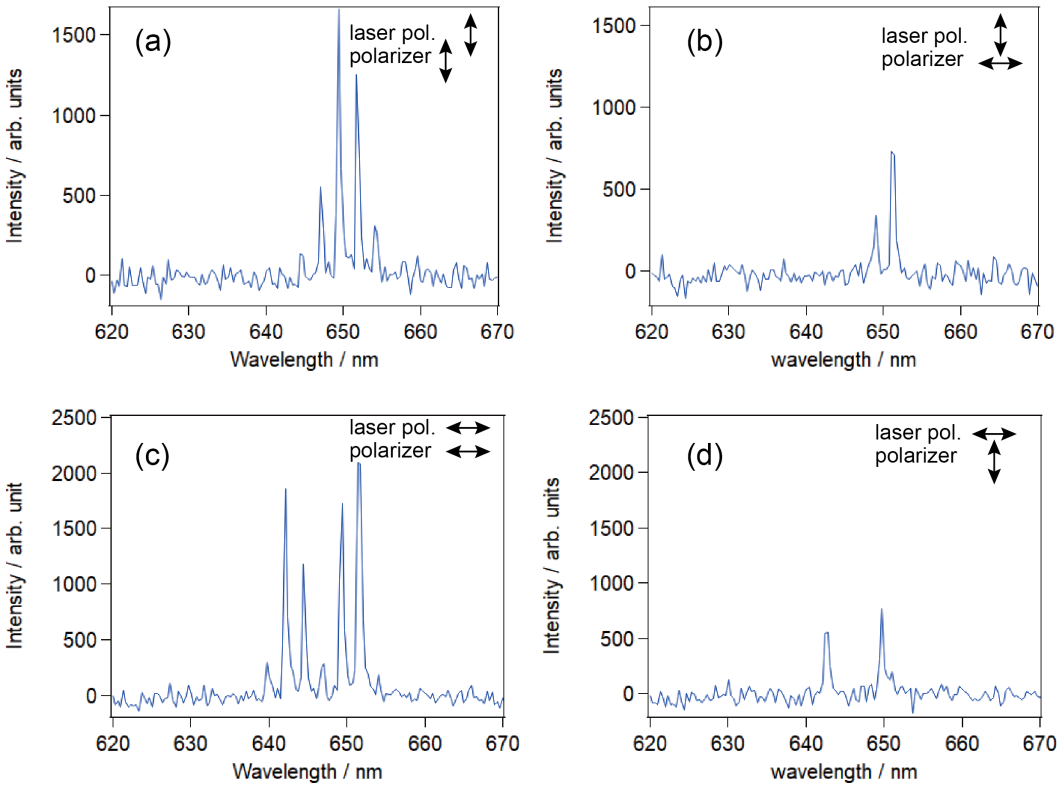

Figure 4-11. Spectra of Raman WGMs observed for a water droplet in different combinations of polarizations for excitation and detection. The horizontal polarization corresponds to the TM mode.

Measurement of time-dependent droplet size of water in a vacuum

The droplet diameter was determined by the following procedure as a function of time. Generation of droplets, excitation by laser pulses, and acquisition of the Raman spectrum were synchronized to TTL pulses by a digital delay generator (DG645, Stanford Research Systems) with a repetition rate of 5 Hz. Whispering gallery mode spectra were obtained shot-to-shot as a function of time elapsed after droplet generation (100–4000 μs). Generation of water droplets in a vacuum lasts approximately for one hour in the present method; it is terminated primarily due to occurrence of bubbles within the nozzle. Bubbles emerge as a result of the reservoir pressure nearly equivalent to the saturated vapor pressure of water. The OH-band Raman spectra measured in this study exhibit structured peaks derived from whispering gallery mode, whereas spontaneous Raman band is not discernible within the experimental signal-to-noise [45, 46]. The WGM wavelengths and FSR were obtained through Gaussian fitting of the spectra.

The droplet size is calculated from WGM resonances based on equation (1). The observed WGM resonances belong almost to a single radial mode. The radial-mode number is reported to increase from 1 to 2 with droplet size from 10 to 50 μm [30, 48]. In this study, radial modes of $l = 1$ and 2 were calculated to reproduce the resonance lines observed experimentally, where a hypothesis of $l = 2$ was adopted by referring to previous reports [30, 47]. As for the polarization of WGMs, the TE mode was selectively measured. The temperature dependence of the refractive index was taken into account based on the cooling rate estimated by the Knudsen equation [5, 48], which employs a given initial diameter and an initial temperature measured at the nozzle tip. The temperature measurements by Raman OH stretching bands and by the Knudsen model agree well with each other as has been reported previously [1, 2]. For taking into account the thermal

conduction inside the droplet, droplets are virtually dividing into 100 shells. The temperature of the droplet surface was employed because, in the ray optics approximation, the WGMs are represented by successive internal total reflection near the surface of the microcavity. The initial diameter was determined by iterative self-convergence.

The droplet size as a function of time is shown in Figure 4-12. Just after its generation from the dispenser head, the quadrupolar vibration was observed as oscillation of the droplet diameter before 900 μs. The quadrupolar vibration of droplets was also observed in detail by measuring the aspect ratio through a high-speed camera (see Section 5-1). The linear fitting of the droplet size beyond 900 μs resulted in an evaporation rate of 0.22 μm/ms with a standard deviation of 0.07 μm/ms. From the damping time constant and the oscillation frequency, the droplet size in the equatorial plane was calculated from Eqs. (4-4-3 and 4) as shown in Figure 4-13. After 700 μs, the amplitude of the oscillation is on the order of 0.01 μm or less, which can be ignored. Prolate droplets with a major axis ~2 μm longer than the minor axis, where substantial deformation of water droplets was expected, were not captured in the WGM measurements. The shrinkage of the droplet can be simulated by the Knudsen equation as described elsewhere [5].

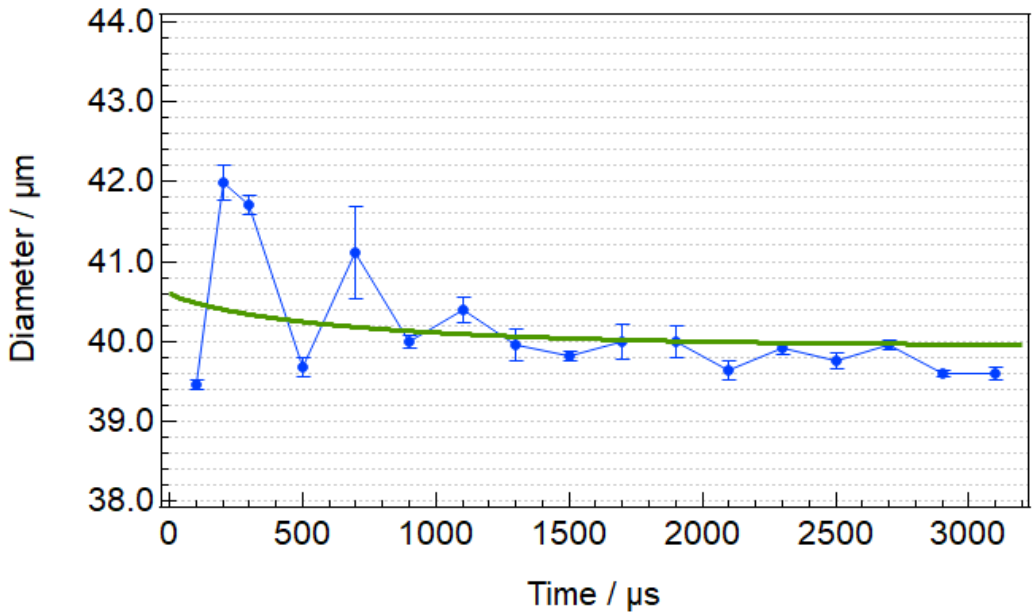

Figure 4-12. Droplet size as a function of time. The diameter determined from the whispering gallery modes in the Raman OH band. The error bars represent standard errors. The solid curve shows prediction by the Knudsen evaporation model with an evaporation coefficient of unity. The initial conditions of the diameter and the temperature were 40.6 µm and 280.45 K, respectively.

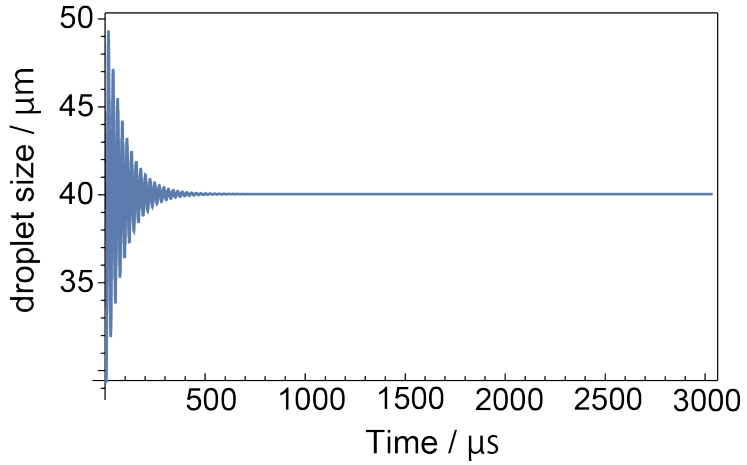

Figure 4-13. Simulation of droplet size as a function of time in the equatorial plane. The damping time constant and the oscillation frequency are 85.6 µs and 252.6 kHz, respectively. The initial droplet diameter was set to 40 µm.

4-4. Freezing time of water droplets in a vacuum

Homogeneous ice nucleation rate of water

Water droplets in a vacuum are suitable for studying freezing of water via homogeneous ice nucleation. Generally, ice nucleation can be classified into either heterogeneous or homogeneous. As a small sample size suppresses heterogeneous nucleation sites, water droplets as small as 40 μm in diameter can persist a liquid state down to homogeneous ice nucleation temperature. Ice formation in a vacuum due to homogeneous nucleation has been reported by state-of-the-art experiments employing X-ray spectroscopy, OH-band Raman spectroscopy, and laser scattering [2, 4, 5]. The homogeneous ice formation is a stochastic process, where the nucleation rate increases with a decrease of 1 K around the temperature of homogeneous ice nucleation [4, 5]. Homogeneous ice nucleation rates are reported in an ambient gas and in inverse (water-in-oil) emulsions [16, 49].

The experiment was conducted using 39.4-μm water droplets in a vacuum. The droplets were cooled down evaporatively, of which size and temperature decreased as they traveled further from the nozzle. The droplet sizes were measured from WGMs of Raman scattering signal in the OH stretching band at 4.0 ms before freezing. The estimation of the temperature was based on the Knudsen theory of evaporative cooling applied to a droplet initially at the nozzle temperature (280.5 K). The fraction of ice-containing droplets increased as a function of time elapsed after droplet generation. The CNN (convolution neural network) was employed for sorting out images of ice from those of liquid to evaluate a fraction of frozen droplets.

The experimental procedure to obtain a scattering image of droplets is as

follows. Light scattered at 90° from a droplet illuminated by a 532-nm CW laser (spot size: 1 mm) was recorded with a CMOS camera (IMX-249, Sony Group Corp.). A microscope telecentric objective lens (Mitsutoyo Corp.) was employed, resulting in a field of view of 1 mm × 0.8 mm. Flight time of a droplet was measured by superimposing a bright field image captured with a 5-μs strobe LED synchronized with the nozzle. The exposure time is sufficiently longer than 1 ms, which is the duration for a water droplet to pass through the field of view. A typical image is shown in Figure 4-14.

The images were classified into intact-liquid and ice-containing droplets according to the following criteria; thereafter, the process was automated through machine learning. Liquid/ice discrimination was carried out by observing laser-scattering and bright-field images. In laser scattering, a liquid droplet shows two streamlines; optical paths for a liquid droplet are clearly shown in Ref.[50]. In contrast, an ice-containing droplet includes random scattering due to expected formation of dendritic ice. Freezing of supercooled water droplets starts with dendritic growth after homogeneous ice nucleation [10, 14]. The freezing velocity of 150-μm drops of supercooled water at –35°C was reported to be 30 cm/s [14]. Therefore, the time interval from ice nucleation to dendritic-ice formation is predicted to be less than 50 μs, which is safely neglected here. The first kink of the trajectory was also the criterion for finding the freezing time. The deflecting trajectory of an ice-containing droplet was expected to be due to non-uniform temperature of the droplet surface causing symmetry breaking in evaporation rates [9]. 500 images were acquired at each flight time, which were classified by using a CNN model that was retrained with previously measured droplet images. The details of the CNN model will be explained in the next section. The fraction of ice-containing droplets thus calculated as a function of time is shown in Figure 4-15. The fraction of ice-

containing droplets rapidly increased within 1300 μs for water droplets with a diameter of 39.4 μm.

The volume-based homogeneous ice nucleation rate (J_v) was calculated from the frozen fraction f_{ice} of droplets as demonstrated in other nucleation studies [5, 13, 20, 23]. The probability $P_x(\Delta t)$, where x-times of ice-nucleation events occur in a droplet with a volume V during a time interval Δt, can be expressed by the following Poisson distribution:

$$P_x(\Delta t) = \frac{(J_v(T)V\Delta t)^x}{x!} \exp\left[-J_v(T)V\Delta t\right] \quad (4\text{-}5\text{-}1)$$

where $J_v(T)$ is the volume-based homogeneous ice nucleation rate at temperature T. On the premise that a droplet starts freezing immediately after an ice nucleus is formed, we may replace $P_{x=0}(\Delta t)$ by $1 - f_{ice}$. The equation for the frozen fraction f_{ice} can be rearranged as an equation for $J_v(t)$:

$$J(t_n) = -\frac{\ln[(1 - f_{ice}(t_{n+1}))/(1 - f_{ice}(t_n))]}{V_{droplet} \times (t_{n+1} - t_n)} \quad (4\text{-}5\text{-}2)$$

where $V_{droplet}$ is the droplet volume and subscripts n and n+1 represent successive measurements. The temperature of the droplet as a function of time is calculated from the Knudsen theory of evaporative cooling. According to the result of cooling calculation, the variability in initial temperatures becomes small in the vicinity of the temperature of homogeneous ice nucleation. For instance, in the case of a 2 K difference in initial temperatures, minor discrepancy of 0.04 K is predicted at 240 K droplets. It is attributed to the fact that a higher initial temperature of the water droplet leads to increase in the vapor pressure. The cooling rate near the homogeneous ice nucleation temperature is 1.8 $\times 10^3$ K/s. To deal with the effect of the thermal conduction, a model droplet is divided into 100 spherical shells. Such a shell model is often used for analysis of thermal

conductance in water droplets [1, 5, 10]. The details of the model were described elsewhere [5]. The vapor pressure and vaporization enthalpy were calculated by using the equations proposed by Murphy and Koop [51], which were derived from the exponential fit to the data of C_p measured by Archer and Carter [52]. The density was calculated by using the sixth-order polynomial reported by Hare and Sorensen [53]. The thermal conductivity κ was calculated by using the equation proposed by the International Association for the Properties of Water and Steam (IAPWS) [35]. Although the evaporation coefficient remains a topic of discussion, we assumed a value of unity here [54]. We thus obtain an ice nucleation rate ranging from 2.1×10^{7} to 1.6×10^{11} $cm^{-3}s^{-1}$ as the temperature decreases from 234 to 231 K (Figure 4-16). For the temperature of the droplet, a mass-averaged temperature, $T_{ave} = \Sigma_{n=0}^{99} [T_n V_n \rho(T_n)]/m$ was employed (ρ is the density of water). The error in the temperature accounts for the temperature gradient inside the droplet; the temperature is lower at the droplet surface where evaporative cooling takes place. The ice nucleation occurs in the vicinity of the cold surface because the nucleation rate show a rapid increase with decreasing temperature. Furthermore, it contributes also to the fact that the cubic decrease in the shell volume towards the inner part of the droplet. The 95% ice-nucleation events occur in the region within 28% radius beneath the surface of 40 μm droplets, according to the shell model calculations. Therefore, the mass averaged temperature calculated for the outer region from 72-th to 100-th shells is also shown in Figure 4-16 by triangles.

Finally, we show the J_v(T) values derived here in Figure 4-17 together with literature values of J_v(T) from previous experimental studies. Our J_v values were close to the extrapolated values reported for 235–238 K, especially Stöckel et al. The reported value below 232 K show some discrepancy between the data presented by Laksmono [23]

and Hagen et al. [22]. Nonetheless, our values tend to align more closely with the values of Laskmono et al. [23]. Their data were obtained under similar condition of evaporative cooling of ~10 μm droplets, so the agreement with our data is not surprising.

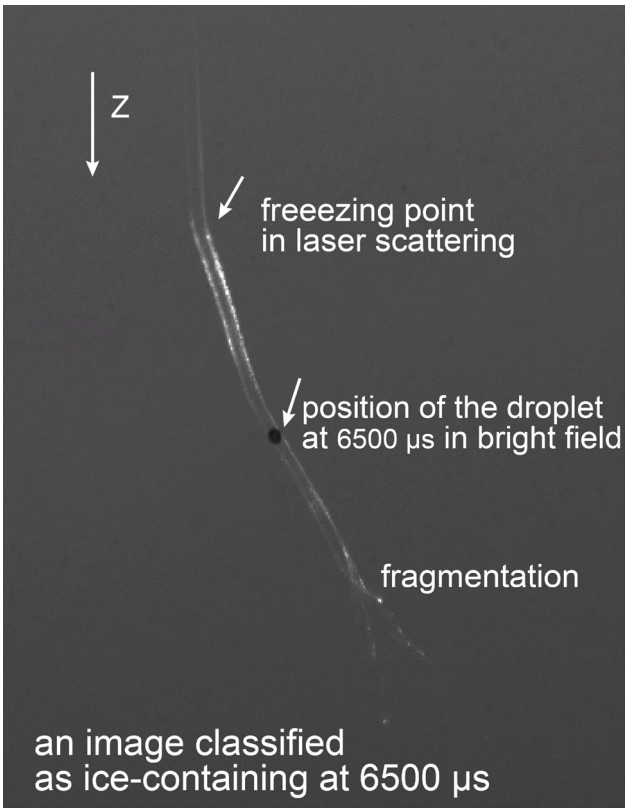

Figure 4-14. A 90° scattered image of water droplet (40 μm) superimposed of bright field of the droplet at 6.5 ms by illuminating the droplet by a strobe LED.

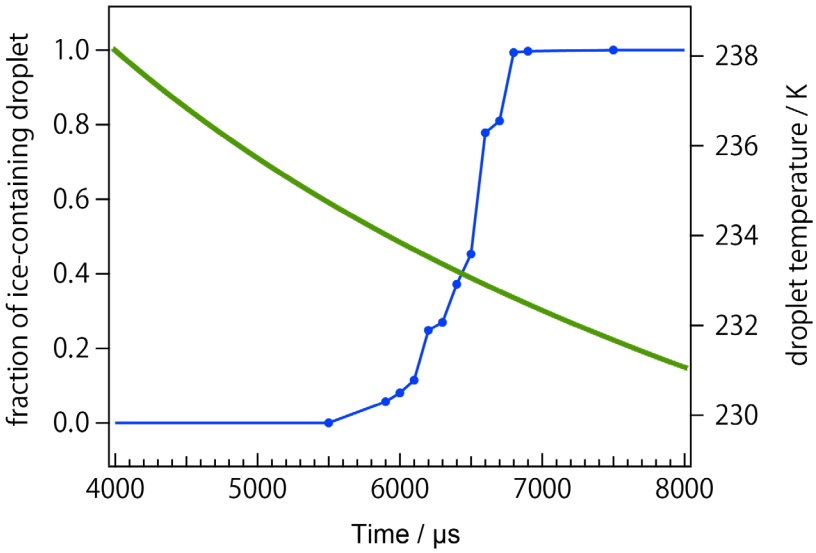

Figure 4-15. The ratio of ice-containing droplets as a function of time in a vacuum for water droplets with diameter of 39.4 μm. The temperature was obtained using the Knudsen theory of evaporation.

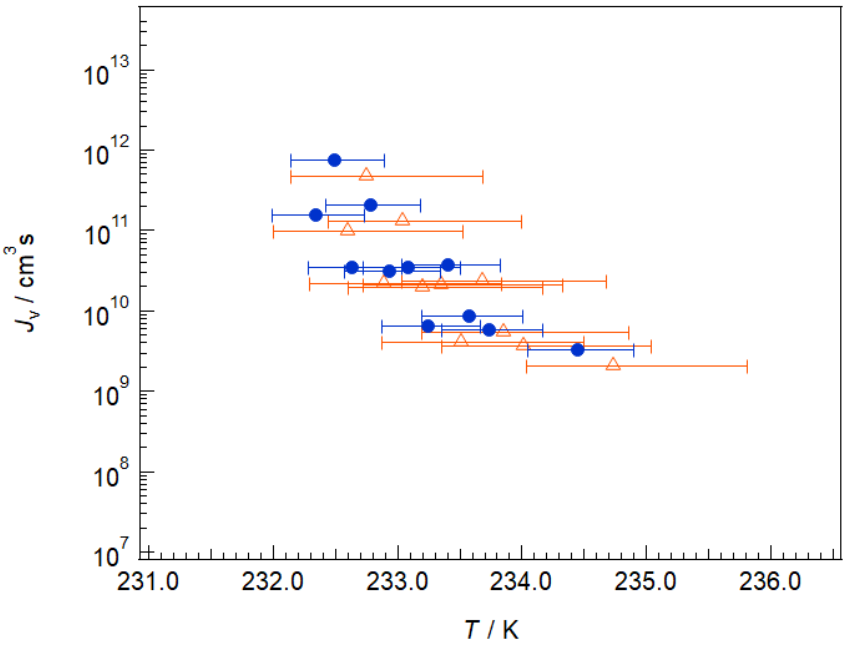

Figure 4-16. Measured volume-dependent homogeneous ice nucleation rate coefficient J_V as a function of temperature within 232–236 K. (triangle) The error bars account for the temperature gradient inside the droplet. The upper/lower limit corresponds to the temperature of the inner-most/surface of the droplet. (ball) The upper/lower limit corresponds to the temperature of the 72th shell/surface (100th shell) of the droplet. The mass averaged temperature was calculated from 72th to 100th shell. The droplet volume was also calculated above 72th shell.

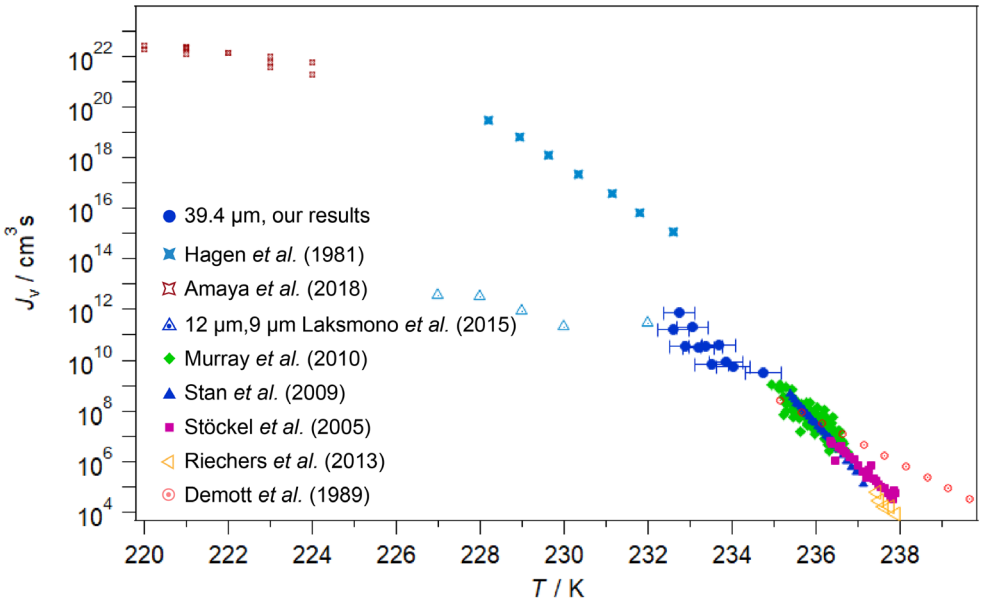

Figure 4-17. Comparison of measured volume-dependent homogeneous ice nucleation rate coefficient *J*v as a function of temperature within 220–240 K.

Deep learning approach: automated recognition of freezing from laser scattering images

Deep learning is a machine learning technique that teaches computers to do what comes naturally to humans: learn by examples. Deep learning is a specialized form of machine learning: deep learning extracts features automatically from images. On the other hand, a machine learning workflow starts with features being manually extracted from images. While deep learning was first theorized in the 1980s [57, 58], there are two main reasons why it has only recently become useful. 1. Deep learning requires large amounts of labelled data. 2. Deep learning requires substantial computing power. Recent advances in deep learning have improved the accuracy in some tasks like classifying objects in images. Most deep learning methods use neural network architectures, which simple models of the way that the human brain processes information. Especially, convolution neural networks (CNN) use 2D convolutional layers, making this architecture well suited to processing 2D data, such as images. In this study, we explored the potential of the CNN models for classifying the image of frozen or liquid water droplets, that is an intriguing example of the application of CNN to the scientific image processing.

Images of ice-containing/water droplets such as Figure 4-14 are classified by using transfer learning from a pre-trained CNN network. Tuning CNN through transfer learning is often faster and easier than constructing and training a new neural network. Most of the pre-trained CNN networks are trained on various image data-sets, notably the ImageNet database [59]. These neural networks have been trained on more than a million images and can classify images into 1000 object categories. Considering the trade-off between accuracy and speed in CNN selection, this study compares the performance of

AlexNet (54% accuracy), Inception-v3 (77%), and NASNet-Large (82%) by using MATLAB (The MathWorks, Inc.). For training data sets, we prepared a 9,100 images sorted categories of water, ice-containing droplets, and unobserved. The categorized 3,900 images were used to evaluate the CNN models after transfer learning. Training cycle was set to 8 epochs and 64 iterations. The results of each model was shown in Table 4-4. The CNN model used for automated classification was Inception-v3 in python-code. The model size (23.9 million parameters) is small while Inception-v3 shows more than 75% accuracy in ImageNet database. Classification took less than 1 s/image and was corrected visually in the end.

CNN model	Validation accuracy	training time /min.	learning rate
AlexNet	82.6%	1.5	0.001
Inception-v3	86.8%	12	0.001
NASNet-Large	91.7%	221	0.001

Table 4-4. Training results of CNN models in transfer learning. The trade-off between training time and accuracy is shown.

References

1. J. D. Smith, C. D. Cappa, W. S. Drisdell, R. C. Cohen, and R. J. Saykally, *J. Am. Chem. Soc.* **128**, 12892 (2006). doi: 10.1021/ja063579v
2. C. Goy, M. A. C. Potenza, S. Dedera, M. Tomut, E. Guillerm, A. Kalinin, K. Voss, A. Schottelius, N. Petridis, A. Prosvetov, G. Tejeda, J. M. Fernández, C. Trautmann, F. Caupin, U. Glasmacher, and R. E. Grisenti, *Phys. Rev. Lett.* **120**, 015501 (2018). doi: 10.1103/PhysRevLett.120.015501
3. M. Faubel, S. Schlemmer, and J. P. Toennies, *Z. Phys. D- Atoms, Molecules and Clusters* **10**, 269 (1988). doi: 10.1007/BF01384861
4. J. A. Sellberg, C. Huang, T. A. McQueen, N. D. Loh, H. Laksmono, D. Schlesinger, R. G. Sierra, D. Nordlund, C. Y. Hampton, D. Starodub, D. P. Deponte, M. Beye, C. Chen, A. V. Martin, A. Barty, K. T. Wikfeldt, T. M. Weiss, C. Caronna, J. Feldkamp, L. B. Skinner, M. M. Seibert, M. Messerschmidt, G. J. Williams, S. Boutet, L. G. M. Pettersson, M. J. Bogan, and A. Nilsson, *Nature* **510**, 381 (2014). doi: 10.1038/nature13266
5. K. Ando, M. Arakawa, and A. Terasaki, *Phys. Chem. Chem. Phys.* **20**, 28435 (2018). doi: 10.1039/c8cp05955a
6. A. J. Heymsfield and L. M. Miloshevich, *J. Atmos. Sci.* **50**, 2335 (1993). doi: 10.1175/1520-0469(1993)050<2335:HINASL>2.0.CO;2
7. D. Rosenfeld and W. L. Woodley, *Nature* **405**, 400 (2000). doi: 10.1038/35013030
8. H. R. Pruppacher, *J. Atmos. Sci.* **52**, 1924 (1995). doi: 10.1175/1520-0469(1995)052<1924:ANLAHI>2.0.CO;2
9. C. A. Stan, A. Kalita, S. Marte, T. F. Kaldawi, P. R. Willmott, and S. Boutet, *Phys.*

Rev. Fluids **8**, L021601 (2023). doi: 10.1103/PhysRevFluids.8.L021601

10. T. Buttersack and S. Bauerecker, *J. Phys. Chem. B* **120**, 504 (2016). doi: 10.1021/acs.jpcb.5b09913
11. A. Lauber, A. Kiselev, T. Pander, P. Handmann, and T. Leisner, *J. Atoms. Sci.*, **75**, 2815, (2018). doi: 10.1175/JAS-D-18-0052.1
12. H. R. Pruppacher, and R. J. Schlamp, *J. Geophys. Res.*, **80**, 380 (1975). doi: 10.1029/JC080i003p00380
13. B. J. Murray, S. L. Broadley, T. W. Wilson, S. J. Bull, R. H. Wills, H. L .Christenson, and E. J. Murray, *Phys. Chem. Chem. Phys.* **12**, 10380 (2010). doi: 10.1039/c003297b
14. C. A. Stan, G. F. Schneider, S. S. Shevkoplyas, M. Hashimoto, M. Ibanescu, B. J. Wiley, and G. M. Whitesides, *Lab Chip* **9**, 2293 (2009). doi: 10.1039/b906198c
15. P. Stöckel, I. M. Weidinger, H. Baumgärtel, and T. Leisner, *J. Phys. Chem. A* **109**, 2540 (2005). doi: 10.1021/jp047665y
16. B. Riechers, F. Wittbracht, A. Hutten, and T. Koop, *Phys. Chem. Chem. Phys.* **15**, 5873 (2013). doi: 10.1039/c3cp42437e
17. P. J. Demott and D. C. Rogers, *J. Atoms. Sci.* **47**, 1056 (1990). doi: 10.1175/1520-0469(1990)047<1056:FNRODS>2.0.CO;2
18. J. Huang and L. S. Bartell, *J. Phys. Chem.* **99**, 3924 (1995). doi: 10.1021/j100012a010
19. A. Manka, H. Pathak, S. Tanimura, J. Wolk, R. Strey, and B. E. Wyslouzil, *Phys. Chem. Chem. Phys.* **14**, 4505 (2012). doi: 10.1039/c2cp23116f
20. A. J. Amaya and B. E. Wyslouzil, *J. Chem. Phys.* **148**, 085401 (2018). doi: 10.1063/1.5019362

21. A. Bhabhe, H. Pathak, and B. E. Wyslouzil, J. Phys. Chem. A **117**, 5472 (2013). doi: 10.1021/jp400070v

22. D. E. Hagen, R. J. Anderson, and J. L. Kassner Jr., *J. Atoms. Sci.* **38**, 1236 (1981). doi: 10.1175/1520-0469(1981)038<1236:HCNRMF>2.0.CO;2

23. H. Laksmono, T. A. McQueen, J. A. Sellberg, N. D. Loh, C. Huang, D. Schlesinger, R. G. Sierra, C. Y. Hampton, D. Nordlund, M. Beye, A. V. Martin, A. Barty, M. M. Seibert, M. Messerschmidt, G. J. Williams, S. Boutet, K. A. Winkel, T. Loerting, L. G. M. Pettersson, M. J. Bogan, and A. Nilsson, *J. Phys. Chem. Lett.* **6**, 2826 (2015). doi: 10.1021/acs.jpclett.5b01164

24. K. Ando, M. Arakawa, and A. Terasaki, *Chem. Lett.* **45**, 961 (2016). doi: 10.1246/cl.160381

25. L. Rayleigh, *Proc. Lond. Math. Soc.* **10**, 4 (1879). doi: 10.1098/rspl.1879.0015

26. L. Rayleigh, *Nature* **44**, 249 (1891). doi: 10.1038/044249e0

27. J. Eggers, *Rev. Mod. Phys.* **69**, 865 (1997). doi: 10.1103/RevModPhys.69.865

28. J. Eggers and E. Villermaux, *Rep. Prog. Phys.* **71**, 036601 (2008). doi: 10.1088/0034-4885/71/3/036601

29. D. P. Deponte, U. Weierstall, D. Starodub, K. Schmidt, J. C. H. Spence, and R. B. Doak, *J. Phys. D: Appl. Phys.* **41**, 195505 (2008). doi: 10.1088/0022-3727/41/19/195505

30. M. Humar, M. Ravnik, S. Pajk, and I. Muševič, *Nat. Photonics* **3**, 595 (2009). doi: 10.1038/NPHOTON.2009.170

31. M. Michihata, A. Kawasaki, A. Adachi, and Y. Takaya, *XXI IMEKO world congress*, (2015).

32. P. Laven, Mie Plot, http://www.philiplaven.com/mieplot.htm, accessed December

2023.

33. J. A. Lock, *J. Opt. Soc. Am. A* **10**, 693 (1993). doi: 10.1364/JOSAA.10.000693
34. J. A. Lock, *Appl. Opt.* **34**, 559 (1995). doi: 10.1364/AO.34.000559
35. IAPWS, R6-95 (2018), http://www.iapws.org/relguide/IAPWS-95.html, access December 2023.
36. D. Duft and T. Leisner, *Int. J. Mass Spectrom.* **233**, 61 (2004). doi: 10.1016/j.ijms.2003.11.020
37. M. Daimon and A. Masumura, Appl. Opt. **46**, 3811 (2007). doi: 10.1364/AO.46.003811
38. B. -C. Damien, *J. Phys. Theor. Appl.* **10**, 198 (1881). doi: 10.1051/jphystap:0188100100019801
39. N. G. Wilson and R. Wright, *J. Phys. Chem.* **35**, 3011 (1931).
40. J. B. Hawkes and R. W. Astheimer, *J. Opt. Soc. Am.* **38**, 804 (1948). doi: 10.1364/JOSA.38.000804
41. Ch. Saubade, *Journal de Physique.* **42**, 359 (1981). doi: 10.1051/jphys:01981004202035900
42. L. Carroll and M. Henry, *Appl. Opt.* **41**, 1330 (2002). doi: 10.1364/AO.41.001330
43. D. R. Lide (ed.), CRC Handbook of Chemistry and Physics, (CRC Press, 2005).
44. R. M. Sayer, R. D. B. Gatherer, R. J. J. Gilham and J. P. Reid, *Phys. Chem. Chem. Phys.*, **5**, 3732 (2003). doi: 10.1039/b304599d
45. L. Mitchem, J. Buajarern, R. J. Hopkins, A. D. Ward, R. J. J. Gilham, R. L. Johnston and J. P. Reid, *J. Phys. Chem. A* **110**, 8116 (2006). doi: 10.1021/jp061135f
46. J. X. Zhang, P. A. Moortgat, and P. M. Aker, *J. Chem. Phys.* **105**, 7276 (1996). doi: 10.1063/1.472588

47. R. D. B. Gatherer, R. M. Sayer, and J. P. Reid, *Chem. Phys. Lett.* **366**, 34 (2002). doi: 10.1016/S0009-2614(02)01531-2

48. M. Knudsen, The Kinetic Theory of Gases: Some Modern Aspects, (Methuen Press, 1950).

49. S. E. Wood, M. B. Baker, and B. D. Swanson, *Rev. Sci. Instrum.* **73**, 3988 (2002). doi: 10.1063/1.1511796

50. A. Ashkin and J.M. Dziedzic, *Appl. Opt.* **20**, 1803 (1981). doi: 10.1364/AO.20.001803

51. D. M. Murphy and T. Koop, *Q. J. R. Meteorol. Soc.* **131**, 1539 (2005). doi: 10.1256/qj.04.94

52. D. G. Archer and R. W. Carter, *J. Phys. Chem. B* **104**, 8563 (2000). doi: 10.1021/jp0003914

53. D. E. Hare and C. M. Sorensen, *J. Chem. Phys.* **87**, 4840 (1987). doi: 10.1063/1.453710

54. M. A. Kazemi, S. H. Zandavi, M. Zargartalebi, D. Sinton, and J. A. W. Elliott, *Int. J. Heat Mass Tranf.* **204**, 123833 (2023). doi: 0.1016/j.ijheatmasstransfer.2022.12383

55. K. Fukushima, *Biol. Cybernetics* **36**, 193 (1980). doi: 10.1007/BF00344251

56. J. J. Hopfield, *Proc. Natl. Acad. Sci.* **79**, 2554 (1982). doi: 10.1073/pnas.79.8.2554

57. ImageNet, https://www.image-net.org/, access January 2024.

Chapter 5. High speed imaging of damping oscillation and fragmentation of water droplets

5-1. Freezing processes of water droplets in a vacuum

For a comprehensive understanding of water droplets in a vacuum, high speed imaging measurements of droplets were performed. During droplet generation, a water droplet gains a surface energy upon separating from bulk water [1]. The surface energy induces oscillatory deformation of the droplet as manifested in high speed images. As the deformation dynamics is governed by surface tension and viscosity of the droplet, it enables contactless measurement of these physical constants. The conventional physical models linking to these material properties are the Rayleigh and Lamb formula [2,3]. However, both equations are derived under weakly damped oscillation. In this study, the linear Navier–Stokes equation was used for a wide damping range to evaluate these properties.

After the water droplet starts damping oscillation upon generation in a vacuum, it undergoes rapid evaporative cooling as well. In the subsequent freezing events, the droplet changes its trajectory [4]. Such deflection in the trajectory is proposed to result from asymmetrical evaporation rates [5]. We captured trajectories of water droplets in a vacuum using a high-speed camera. Also, even fragmentation is predicted for freezing water droplets of 50–70 μm in diameter [4], which is of interest in the context of ice formation. In the atmosphere, the fragmentation of ice droplets is considered as one of the factors contributing to water droplet freezing above the limit for homogeneous freezing [6]. Although the probability for leading to fragmentation varies depending on

reports from different research groups, there is a notable decrease in the fragmentation probability for droplets of 50 μm or less under an ambient pressure [7-10]. A model calculation also predicts absence of fragmentation in water droplets smaller than 50 μm [11]. However, using a high-speed camera, the present observation in a vacuum reveals an enhanced probability of fragmentation even for water droplets as small as 40 μm.

5-2. Damping oscillation of droplets

Oscillation of liquid micro-droplets is a physical phenomenon governed by viscosity, surface tension, and droplet size. For water droplets larger than ~10 μm, oscillation excited upon droplet generation by a piezo-driven dispenser has a non-negligible effect on droplet deformation that affects the size measurement by WGMs. To evaluate an amplitude of oscillation, oscillating droplets were recorded as a movie by a high-speed camera (ACS-1, nac Image Technology Inc.). As described below, the shape descriptors calculated in this study are the diameter, aspect ratio, and roundness. Since the depth of field of the camera was shallow, the oscillatory deformation was characterized solely by the aspect ratio. Figure 5-1 shows an example of a shadowgraph image taken at a rate of 400,000 fps, a resolution of 1280×96, and a exposure time of 1 μs, from which an aspect ratio was calculated by elliptical fitting of the contour of the image to extract the lengths of major and minor axes.

An oscillation manifested in the aspect ratio is shown in Figure 5-2, which was observed for a 42.4-μm water droplet in the atmosphere. The time zero was defined as the time when the water droplet was released from the nozzle. Reproducibility of the oscillatory behavior was confirmed by repeated measurements for multiple droplets with a single-capture mode of a high-speed camera synchronized with a delay generator as shown in Figure 5-3, which exhibits a similarity to Figure 5-2 obtained by a high-speed camera capturing a single droplet. This similarity implies that the present method of droplet generation has sufficiently high reproducibility that allows reliable measurement of the droplet size via WGMs described in Section 4-3.

Oscillating liquid droplets are modeled conventionally by the Rayleigh and

the Lamb formula [2,3]. The oscillation frequency depends on the surface tension and the droplet mass, while the damping time is dependent on the viscosity as well as the droplet mass. Therefore, the frequency and the damping time of surface oscillation has been used for contactless measurements of viscosity and surface tension [12-17]. Both the formula are derived under an assumption of either damping free or very weak damping. Such an ideal oscillation is not realized when an aspect ratio is significantly large (>~1.2) as in the present case (see Figure 5-2). The model has been extended to large-amplitude oscillations as reported by Refs. [18] and [19]. In this study, viscosity η and surface tension γ were calculated based on the basic characteristic equation of the linear Navier–Stokes equation introduced by G. Lohöfer, which represents a model applicable to any damping range [19].

$$\gamma = \frac{3M}{32\pi}{\omega_2}^2 \tag{4-4-1}$$

$$\frac{1}{\eta} = \frac{20\pi a}{3M}\tau_2\left(1 - \sqrt{\frac{18}{125}}\frac{1}{\sqrt{\omega_2\tau_2}}\right) \tag{4-4-2}$$

where ω_2 is the oscillation frequency and τ_2 the damping time of the fundamental mode $l = 2$, M the droplet mass, and a the equilibrium radius of the droplet. Oscillatory deformation of a liquid droplet around the equilibrium point can be described by an infinite series of orthogonal surface spherical harmonics. The radius r changes as a function of time t and polar angle θ as

$$r(t,\theta) = r_0[1 + \frac{1}{2}A_2(t)(3\cos^2\theta - 1)] \tag{4-4-3}$$

where $A_2(t)$ is an instantaneous amplitude of the 2nd oscillation mode normalized by initial radius r_0. $A_2(t)$ is expressed by the aspect ratio ξ as follows:

$$A_2(t) = \frac{\xi(t) - 1}{2 + \xi(t)/2} \tag{4-4-4}$$

The damping time τ_2 and oscillation frequency ω_2 can be extracted from the time dependence of A_2 and its Fourier transform (Figure 5-2). The oscillation frequency at about 40 kHz was split into two components in Figure 5-2(a), which originates from the distortion in the periodic oscillation observed at 140 μs. The oscillation frequency can split into several peaks due to rotational sample movements [16, 20, 21]. The sample rotation was estimated to be 0.83° /s by the elliptical-fitting analysis of the present experimental data. Taking this sample rotation into account, we were able to derive an ideal periodic oscillation as shown in Figure 5-2(b). Inclination from the image plane and rotation about z-axis were ignored. Although the effect of the translational motion is still included, the main peak at 40 kHz appeared as a single peak (the inset of Figure 5-2(b)). The values of surface tension and viscosity calculated from Eqs. 4-4-1 to 4-4-2 are 76.0 mN/m and 1.05 mPa·s, where ω_2:253 kHz and τ_2:8.56×10^{-5} s and the droplet radius was derived to be 21.2 μm from the high-speed image and the density of water at 8.5°C. Compared with the reference data of water at 9°C [22], surface tension and viscosity are 74.37 mN/m and 1.356 mPa·s. The relative error of referenced data are 2% and 20%, respectively.

Damping oscillation was measured also in a vacuum using the same method as in Figure 5-3 performed in the atmosphere. As shown in Figure 5-4, the oscillation can be observed until 200 μs. According to temperature simulation based on the Knudsen theory, the mass averaged temperature of the droplet at 200 μs is 271 K, when initial temperature and diameter are 280 K and 40 μm, respectively. The decrease in temperature from 280 to 271 K leads to an increase in surface tension and viscosity from 74.7 to 75.4 mN/m [23] and from 1.425 to 1.928 mPa·s [24], respectively. The diminishing oscillation beyond 200 μs in Figure 5-4 compared with Figure 5-3 is

speculated to be a result of an increase in viscosity.

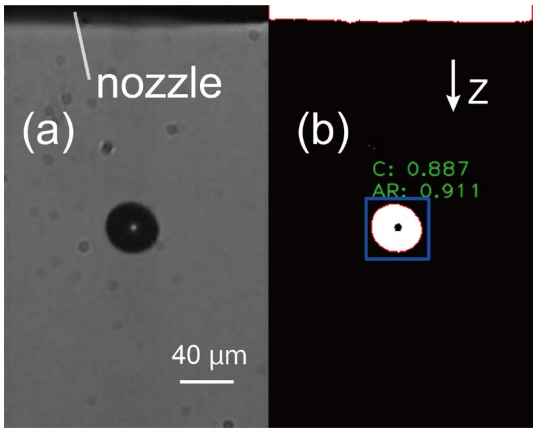

Figure 5-1. (a)8-bit gray scale image of droplet. (b)Binary image of (a) with threshold set to 48, inverted to black and white. The contours of droplet (red line) was fitted with an ellipse, which is used for calculating the aspect ratio (AR) from major and minor axis. The roundness (C) was calculated from the area and length of contours ($4\pi \times \text{area}/\text{Perimeter}^2$).

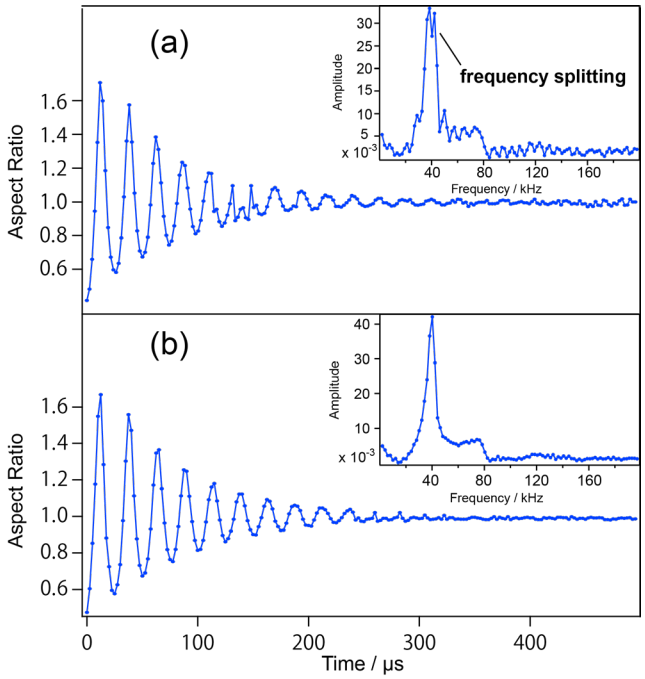

Figure 5-2. Aspect ratio of the droplet as a function of time after the droplet left the nozzle in the atmosphere as measured by high speed imaging (400,000 frames/sec.). (a) Damping oscillation of the droplet as observed. (b) Aspect ratio taking into account an angular velocity of 0.83°/s estimated by elliptical fitting. Corresponding Fourier-transformed spectra are shown in the insets. The exposure time was set to 1 µs.

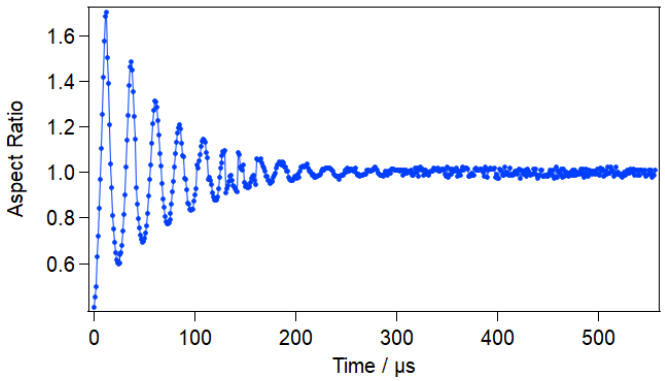

Figure 5-3. Aspect ratio of droplets as a function of delay time between droplet generation at the nozzle and image capture by the camera. Each plot represents a different water droplet captured by varying the delay time. The consistency with Figure 5-2(a) indicates high reproducibility in water droplet generation. The time interval was set to 1 μs. Also, exposure time was set to 1 μs.

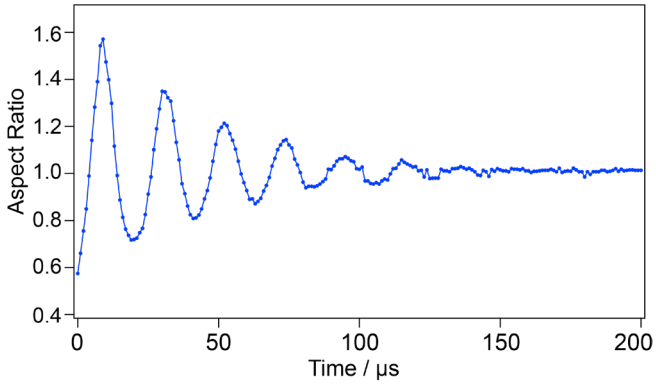

Figure 5-4. Aspect ratio of droplets as a function of time in a vacuum. The pressure of chamber was 1.7 Pa. The initial temperature of water was 6.9 °C. The setup of the camera was the same as Figure.5-3.

5-3. High speed imaging of homogeneous ice formation

The process of water-droplet freezing in a vacuum was also observed by a high-speed camera (ACS-1, nac Image Technology Inc.) in a video mode, which was triggered by a digital delay generator (DG645 ,Stanford Research Systems) at a given time delay from droplet generation. A zoom lens configuration provided a working distance of 97 mm and a range of magnification from ×6.5 to ×23 (Z16 APO and Plan APO and some other components, Leica Microsystems GmbH). The field of view of the camera at the lowest magnification (×6.5) was 3.2 mm × 4.5 mm. The video frame rate was set to 54 kHz. Due to its principle, the practical resolution of a high-speed camera changes depending on the target frame rate. For supporting a high frame rate and a large field of view, images were acquired using bilinear based interpolation methods.

The representative set of images of homogeneously frozen pure water droplets are shown in Figure 5-4(a) at 8-frame intervals. The fact that the droplet images are not equally spaced at each interval indicates that the water droplet undergoes irregular acceleration. Ice spicules are observed at 6.9 ms that grow up further; similar events were confirmed in almost all the droplets examined. The spicules have been reported both in an ambient pressure and in a vacuum during the freezing stage of homogeneous ice nucleation [9, 11, 25]. High speed recording by Wildeman et al. shows that the spicules are formed by freezing of water subsequent to being pushed out of the ice shell through a small crack [11]. Formation of an ice shell is observed after the dendritic ice growth by a high speed camera [11, 26]. It is noteworthy that images of 50-μm frozen droplets show the presence of spicules in homogeneous freezing, while heterogeneous ice nucleation at –8°C of the same size shows no spicules or deformation [25]. From this report, spicules

are considered to be a characteristic geometry in homogeneous ice nucleation of water droplets around 40 μm. However, spicule formation is reported also for heterogeneous freezing, where droplets freeze into polycrystalline ice; spicules are formed with a probability of 90–100% in this case [27, 28]. It is speculated that ice droplets observed in the present experiment are also polycrystalline in view of the high probability of spicule formation.

The flight trajectory of a droplet changes its direction after ice nucleation. Such a spontaneous motion of free droplets freezing is also reported in other studies [4, 11]. Recently, a simplified evaporation model by C. A. Stan et al. [5] proposed an asymmetric evaporative flux, from which a droplet experiences a net reactive force directed opposite to the nucleation point. In this study, flight trajectories were observed using a high-speed camera. Also, spicule growth and angular velocity increase were confirmed after deflection. The change in the angle of spicules indicates a rotational velocity of 1.3°/μs; this means that the angular velocity increases with respect to < 0.83°/μs just after droplet generation as estimated from the damping oscillation.

Fragmentation of water droplets smaller than 50 μm have not been reported before [6, 7, 9, 25]. From the simple theoretical model of kinetic-energy balance, Wildeman et al. [11] predicted that symmetrically freezing droplets smaller than 50 μm in diameter cannot break up. However, fragmentation of ice droplets as small as 42 μm was observed for most of the droplets examined in the present study. Figure 5-5 shows several images of fragmentation events. . It was observed that, out of 128 freezing events, 85% of droplets break up within the field of view. These events include 73% of splitting into approximately equal two fragments, 10% of splitting into three, and 2% of splitting into four. The mean fragmentation time (time elapsed from ice nucleation to

fragmentation) is calculated to be 674±106 μs, which is derived by assessing the time interval between the first kink of the trajectory and the onset of fragmentation. From the laser scattering pattern as shown in Figure 4-14, the onset of freezing coincides with the irregular deflection of the trajectory. The fragmentation time predicted by Wildeman et al. is ~10 ms at 50 μm droplets, which is more than 10 times longer than the present observation (674 μs) for 40-μm droplet. The model calculation reported by Wildeman et al. assumes that the increase in the internal pressure is occasionally released by multiple cracks. However, in the case of nucleation following rapid evaporative cooling as in this study, the internal pressure due to the growth of an ice shell may have surpassed the pressure release through cracking. The fragment velocity, excluding the initial velocity of the droplet was 2.1 m/s, which is slightly faster than 1.0 m/s reported by Wildeman et al. [11].

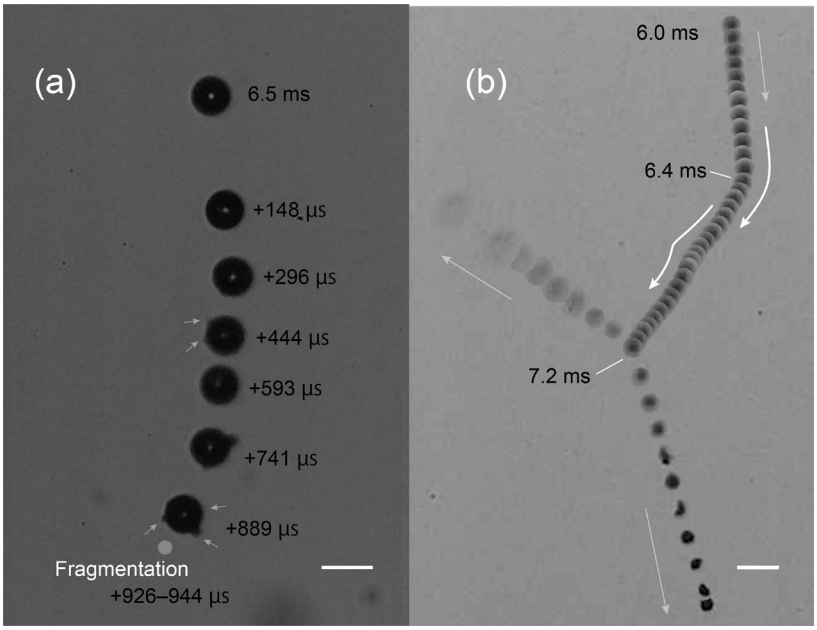

Figure 5-4. High speed microscopy images of freezing water droplets in a vacuum. (a) Ice spicules and deformation are captured at around 6.9 ms (the image indicated as +444 µs). The magnification was set to ×23 (Scale bar: 50 µm). (b) Spontaneous trajectory deflection and subsequent fragmentation were observed. The magnification was ×6.25 (Scale bar: 100 µm).

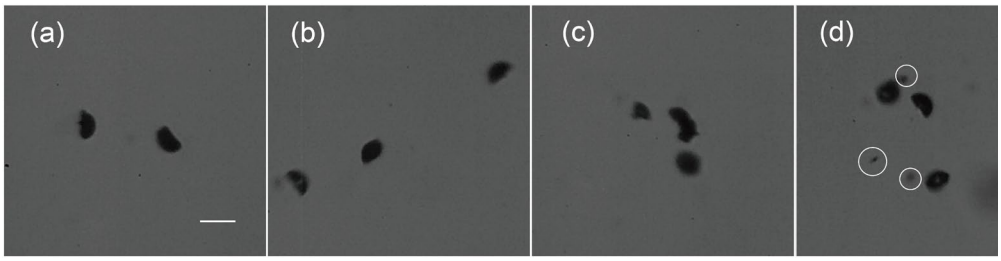

Figure 5-5. Fragmentation of droplets. (Scale bar: 50 µm) (a) Most of the droplets break up into two fragments. In some cases, (b) three and (c) four fragments were observed. (d) Occasionally, small fragments were observed.

References

1. G. Brenn and A. Frohn, *Exp. Fluids* **15**, 85 (1993). doi: 10.1007/BF00190947
2. H. Lamb, *Proc. Lond. Math. Soc.* **1**, 51 (1881). doi: 10.1112/plms/s1-13.1.51
3. L. Rayleigh, *Proc. R. Soc. Lond.* **29**, 71 (1879).
4. K. Ando, M. Arakawa, and A. Terasaki, *Phys. Chem. Chem. Phys.* **20**, 28435 (2018). doi: 10.1039/c8cp05955a
5. C. A. Stan, A.. Kalita, S. Marte, T. F. Kaldawi, P. R. Willmott, and S. Boutet, *Phys. Rev. Fluids* **8**, L021601 (2023). doi: 10.1103/PhysRevFluids.8.L021601
6. A. Lauber, A. Kiselev, T. Pander, P. Handmann, and T. Leisner, *J. Atoms. Sci.* **75**, 2815, (2018) doi: 10.1175/JAS-D-18-0052.1
7. P. V. Hobbs and A. J. Alkezweeny, *J. Atmos. Sci.* **25**, 881 (1968). doi: 10.1175/1520-0469(1968)025<0881:TFOFWD>2.0.CO;2
8. C. Takahashi*, J. Meteorol. Soc. Jpn.* **53**, 402 (1975). doi: 10.2151/jmsj1965.53.6_402
9. M. L. López and E. E. Ávila, *Geophys. Res. Lett.* **39**, L01805 (2012). doi: 10.1029/2011GL050185
10. D. A. Johnson and J. Hallett, *Q. R. J. Meteorol. Soc.* **94**, 468 (1968). doi: 10.1002/qj.49709440204
11. S. Wildeman, S. Sterl, C. Sun, and D. Lohse, *Phys. Rev. Lett.* **118**, 084101 (2017). doi: 10.1103/PhysRevLett.118.084101
12. D. L. Cummings and D. A. Blackburn, *J. Fluid Mech.* **224**, 395 (1991). doi: 10.1017/S0022112091001817
13. I. Egry, H. Giffard, and S. Schneider, *Meas. Sci. Technol.* **75**, 4043 (1995). doi: 10.1088/0957-0233/16/2/013

14. W. Rhim, K. Ohsaka, P. Paradis, and R. E. Spjut, *Rev. Sci. Instrum.* **70**, 2796 (1999). doi: 10.1063/1.1149797
15. T. Matsumoto, T. Nakano, H. Fujii. M. Kamai, and K. Nogi, *Phys. Rev. E* **65**, 031201 (2002). doi: 10.1103/PhysRevE.65.031201
16. Y. Sun, H. Muta, and Y. Ohishi, *Microgravity. Sci. Technol.* **33**, 32 (2021). doi: 10.1007/s12217-021-09883-7
17. Y. Wu, Q. Lv, X. Wu, X. Wang, L. Chen, and K. Cen, *Powder Technology* **391**, 425 (2021). doi: 10.1016/j.powtec.2021.06.029
18. O. A. Basaran, *J. Fluid. Mech.* **241**, 169 (1992). doi: 10.1017/S002211209200199X
19. G. Lohöfer, *Int. J. Thermophys.* **41**, 30 (2020). doi: 10.1007/s10765-020-2608-z
20. F. H. Busse, *J. Fluid. Mech.* **142**, 1 (1984). doi: 10.1017/S0022112084000963
21. I. Egry, H. Giffard, and S. Schneider, *Meas. Sci. Technol.* **16**, 426 (2005). doi: 10.1088/0957-0233/16/2/013
22. D.R. Lide (Ed.), CRC Handbook of Physics and Chemistry, 82nd ed., CRC Press, (2001).
23. P. T. Hacker, Technical Note 2510, National Advisory Committee for Aeronautics, (1951).
24. A. Dehaoui, B. Issenmann, and F. Caupin, *Proc. Natl. Acad. Sci.* **112**, 12020 (2015). doi: 10.1073/pnas.1508996112
25. S. E. Wood, M. B. Baker, and B. D. Swanson, *Rev. Sci. Instrum.* **73**, 3988 (2002). doi: 10.1063/1.1511796
26. T. Buttersack, and S. Bauerecker, *J. Phys. Chem. B* **120**, 504 (2016). doi: 10.1021/acs.jpcb.5b09913
27. C. Takahashi , *J. Meteor. Soc. Japan* **54**, 448 (1976).

doi: 10.2151/jmsj1965.54.6_448

28. R. L. Pitter and H. R. Pruppacher, *Quart. J. R. Met. Soc.* **99**, 540 (1973). doi: 10.1002/qj.49709942111

Chapter 6 Whispering gallery modes in broadband coherent anti-Stokes Raman scattering

Multiplex coherent anti-stokes Raman scattering (CARS) has been applied to obtaining fundamental vibrational modes of biological cells by expanding the bandwidth of the Stokes radiation [1, 2]. Especially, the spectral coverage of multiplex CARS using supercontinuum generated from a photonic crystal fiber extends even over 2500cm^{-1} [3]. The continuous spectra of multiplex CARS exhibit not only vibrational resonances but also non-resonant background signals [4], which is an advantage in measurements of whispering gallery modes (WGMs). The WGMs obtained by broadband multiplex CARS in spherical objects are expected to be useful in analyzing complex Mie theories, which provide the size of the object and the refractive index of the material along with its wavelength dispersion. In this study, the whispering gallery modes of 10-μm polystyrene beads (Polybead microspheres, Polysciences, Inc.) were measured by employing an ultrabroadband multiplex CARS spectroscopic imaging system.

The experimental setup of multiplex CARS has been described elsewhere [5, 6]. Briefly, the main light source was a custom-made dual-fiber output synchronized laser (OPERA HP, Leukos, Limoges, France). The dual outputs from the laser (pump beam: 1064 nm, Stokes beam: ultra-broadband supercontinuum radiation ranging from visible to near infrared) were superimposed using a notch filter and were guided into a modified inverted microscope in a collinear geometry. The polystyrene beads were supported on a glass slide surrounded by the air. The sample slide glass was placed on a piezoelectric stage for three-dimensional adjustment. The multiplex CARS signal was detected by a spectrometer equipped with a CCD camera.

The CARS spectra obtained by irradiating the center and the edge of the beads are shown in Figures 6-1 and 6-2, respectively. The vibrational bands were assigned based on Raman-shift values [5]. The CARS signals originating from the center of the polystyrene bead (Figure 6-1(b)) diminish as the irradiation position of the laser is displaced toward the edge, where only the WGM resonances are observed (Figure 6-2(b)). These signals were not observed outside the bead area.

The WGMs observed in the non-resonant CARS signal region are assigned as shown in Figure 6-2(b). Two distinct series of WGMs were discernible, which were ascribed to WGMs from the two beads located at the right and the upper side of the laser position indicated in Figure 6-2(a). The size of the beads were evaluated to be 10.43 and 10.76 μm for the right and the upper beads, respectively, which were within the range of 10 ± 1 μm described in the datasheet of the polystyrene beads purchased. The pump and Stokes beams in TM polarization for the right bead become TE polarization for the upper bead. Simultaneous observation of orthogonal TM and TE polarizations further supports these results. The profile of the WGM signal intensity would not be addressed here, which is influenced by experimental conditions such as the calibration of the spectrometer and the chirping properties of the Stokes laser.

The multiplex CARS provide WGMs in a wavelength range broader than that for an ordinary Raman band in Section 4. The broadband WGMs would have an advantage in the measurement of refractive-index dispersion and its temperature dependence with high precision. For example, the refractive-index dispersion has been reported for polystyrene beads [7, 8]. The benefits of broadband WGMs are not limited to polystyrene beads but can be applied to supercooled water droplets as well. So far, a refractive index of supercooled water has been reported in the wavelength range between

534 and 675 nm by spectroscopic approaches [9, 10]. However, its temperature dependence has not yet been reported as far as we know. It is expected that future studies will elucidate temperature dependence of the refractive-index dispersion of supercooled water by taking advantages of multiplex CARS to obtain WGMs in broadband.

In summary, WGMs have been measured for 10-μm polystyrene beads by broadband multiplex CARS. The CARS spectrum of the polystyrene beads show non-resonant background signals as well as several peaks attributable to the molecular vibrations of polystyrene. By adjusting the pump- and Stokes-beam positions to the edge of the beads, WGMs from non-resonant background were observed, which was assigned to 10 radial modes. The size of the beads was calculated from the observed WGMs using the Mie theory, resulting in 10.43 and 10.76 μm for two beads. Broadband WGMs hold the potential for acquiring wavelength dispersion. In the future, WGMs via broadband multiplex CARS could serve a method for simultaneous measurement of the temperature-dependent size changes due to thermal expansion/shrinking and the wavelength dispersion of refractive index.

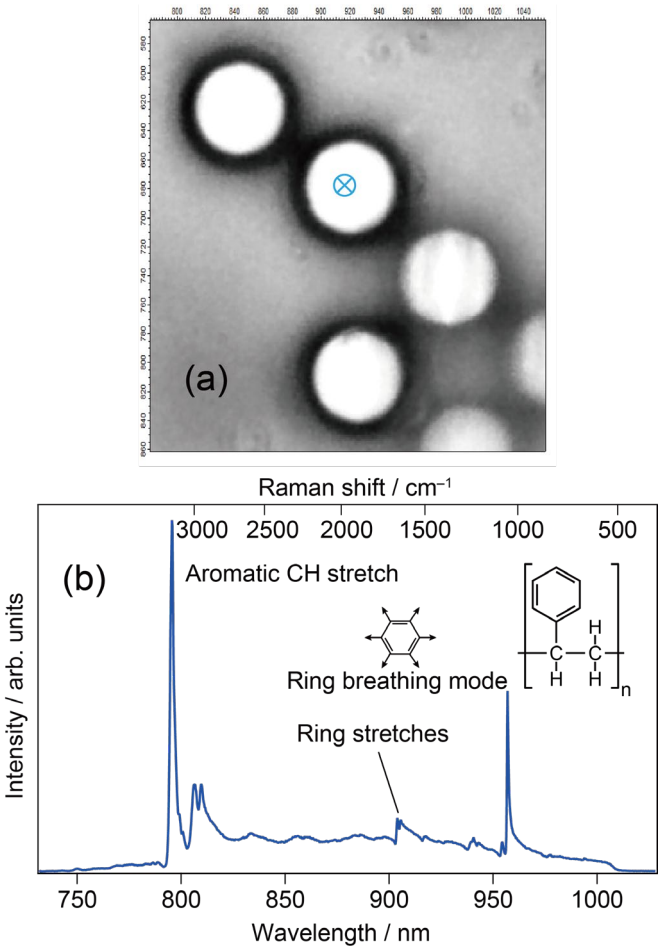

Figure 6-1. Ultrabroadband multiplex CARS from a polystyrene bead. (a) The position of the pump and the Stokes lasers. (b) The CARS spectrum of a polystyrene bead. For comparison with Figure 6-2(b), the abscissa is represented in wavelength.

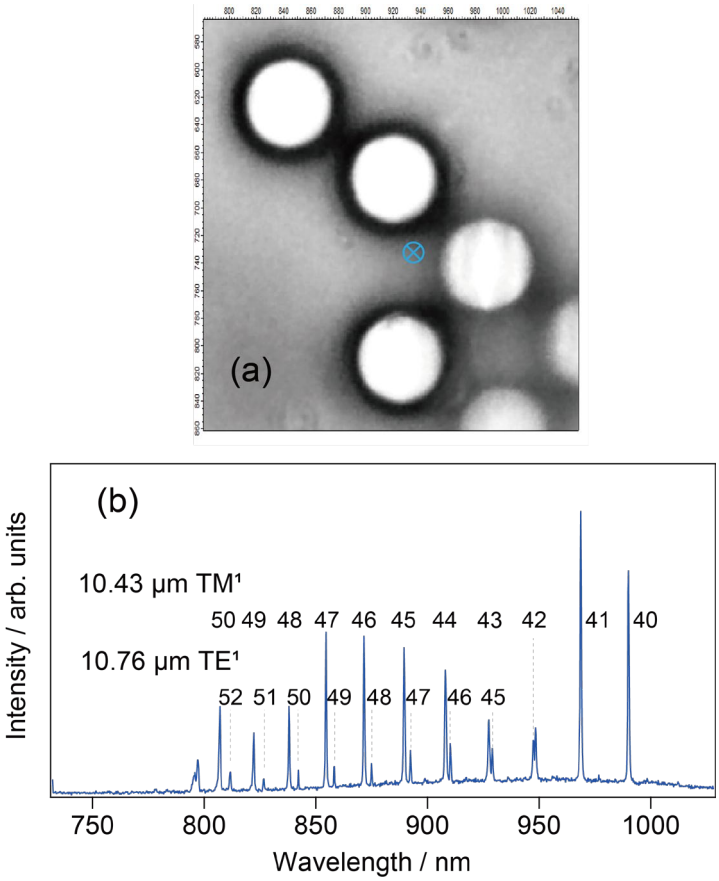

Figure 6-2. Whispering gallery modes observed for two polystyrene beads. (a) A microscopy image of polystyrene beads. The bule circle shows the position of the laser. (b) A spectrum of WGMs measured at the position shown in (a). TM and TE modes correspond to signals from the right and the upper beads, respectively; i.e., the electric vector of the laser polarization is horizontally aligned.

References

1. B. N. Toleutaev, T. Tahara, and H. Hamaguchi, *Appl. Phys. B* **59**, 369 (1994). doi: 10.1007/BF01081059
2. M. Müller and J. M. Schins, *J. Phys. Chem. B* **106**, 3715 (2002). doi: 10.1021/jp014012y
3. H. Kano and H. Hamaguchi, *Apply. Phys. Lett.* **86**, 121113 (2005). doi: 10.1063/1.1883714
4. H. A. Rinia, M. Bonn, and M. Müller, *J. Phys. Chem. B* **110**, 4472 (2006). doi: 10.1021/jp0564849
5. H. Yoneyama, K. Sudo, P. Leproux, V. Couderc, A. Inoko, and H. Kano, *APL Photonics* **3**, 092408 (2018). doi: 10.1021/jp0564849
6. K. Tanaka, R. Oketani, T. Terada, P. Leproux, Y. Morono, and H. Kano, *J. Phys. Chem. B* **127**, 1940 (2023).
7. S. H. Jones, M. D. King, and A. D. Ward, *Phys. Chem. Chem. Phys.* **15**, 20735 (2013).
8. J. B. Bateman, E. J. Weneck, and D. C. Eshler, *J. Colloid Sci.* **14**, 308 (1959). doi: 10.1016/0095-8522(59)90055-8
9. D. Duft and T. Leisner, *Int. J. Mass Spectrom.* **233**, 61 (2004). doi: 10.1016/j.ijms.2003.11.020
10. C. Goy, F. Caupin, M. Caresana, L. Cremonesi, A. Kalinin, G. Grübel, M. A. C. Potenza, and R. E. Grisenti, *J. Phys. Chem. Lett.* **13**, 11872 (2022). doi: 10.1021/acs.jpclett.2c02803

Chapter 7. Concluding remarks

In the present work, experimental and computational approaches were proposed for the studies of ion-beam manipulation and droplet dynamics. The computational method implemented in the SIMION software for solving Laplace's equation provides ion trajectories along the entire time-of-flight mass spectrometer. Here the author presented a novel design of a reflectron equipped with an additional electrostatic lens in front of a conventional ion reflector for improving convergence of an ion beam. The computational ion beam evaluation of the entire device, exceeding 1 m in size, provides clear guideline for electrode design. Its superior performance was demonstrated by chemical reaction experiments and X-ray spectroscopy. In addition, ion trajectory simulations for linear ion traps were performed to characterize an ion cloud created by stored ions. Ion-distribution profiles that have been reported by experiments were quantitatively reproduced by incorporating the effects of space charge and buffer-gas thermalization. The present simulation method has a potential for future applications to various ion-trap simulations. Finally, the size of evaporating water droplets injected into a vacuum has been probed via WGMs observed in the OH stretching band of the Raman scattering spectrum. The droplet size as a function of time showed damping oscillation of quadrupolar distortion and shrinkage due to evaporation. Subsequent freezing events were monitored by a high-speed camera. Computer analysis employing Mie theory and image processing demonstrated its capability to derive the evaporation rate and the homogeneous freezing nucleation rate of supercooled water. Particularly, we anticipate future experiments that will validate the results of homogeneous ice nucleation rates below 235 K with the outcomes of our present study. Fragmentation of water droplets was induced even for sizes as small as 50 μm. The material properties of supercooled

water droplets measured in this study contribute to a better understanding of the complexities within the depth of supercooling.

List of principal publications

1. **Takefumi Handa, Takuya Horio, Masashi Arakawa and Akira Terasaki,** "Improvement of reflectron time-of-flight mass spectrometer for better convergence of ion beam", *Int. J. Mass Spectrom.* **451**, 116311/1-5 (2020). doi: 10.1016/j.ijms.2020.116311

2. **Takefumi Handa and Akira Terasaki**, "Ion trajectory simulation of linear multipole ion traps for analysis of spatial ion distribution", *Mol. Phys.* **121**, e2259013/1-7 (2023). doi: 10.1080/00268976.2023.2259013

3. **Takefumi Handa, Masashi Arakawa, Takuya Horio and Akira Terasaki,** "Homogeneous ice nucleation rates of supercooled water droplets evaporating in a vacuum: Droplet size measurement via whispering gallery modes", in preparation

4. **Takefumi Handa, Yuta Suzuki, Masashi Arakawa, Takuya Horio and Akira Terasaki,** "High speed imaging of damping oscillation and fragmentation of water droplets in a vacuum", in preparation

List of other publications

1. **Tetsuichiro Hayakawa, Masashi Arakawa, Satoshi Kono, Takefumi Handa, Naho Hayashi, Kento Mimamikawa, Takuya Horio and Akira Terasaki** "X-ray absorption spectroscopy of small copper-oxide cluster ions for analyses of Cu oxidation sate and Ar complexation: $CuOAr^+$ and $Cu_2O_2^+$," *Z. Phys. Chem.* **235**, 213-224 (2021). doi: 10.1515/zpch-2020-1668

2. **Takefumi Handa, Takuya Horio, Masashi Arakawa and Akira Terasaki** "Development of reflectron time-of-flight mass spectrometer for improving ion-beam convergence" (in Japanese), *Bull. Soc. Nano Sci. Tech.* **21**, 17-22 (2022).

Acknowledgments

This work was supported financially by the Japan Society for the Promotion of Science (JSPS) KAKENHI [grant numbers JP21J21716, JP22H00317, JP17H06456 and JP21K18604]. I would like to express my sincere gratitude to Professor Kano and grad. student Tanaka for providing the data on multiplex CARS of polystyrene beads in Chapter 6.

I would like to show my greatest appreciation to my advisors, professor Akira Terasaki, associate professor Horio Takuya, and assistant professor Masashi Arakawa, for their invaluable guidance, and commitment to my academic and research endeavors throughout the entirety of my doctoral studies. Their expertise and constructive feedback have been instrumental in shaping the trajectory of my research. Especially, the relationship to my Prof. spans an nine years, making it the longest, after that with my parents, the most significant connection in my life.

I would like to express my heartfelt gratitude to Masato Yamaguchi, who was a special assistant professor at the time, for contributions to my academic growth during our interaction. I extend my thanks to Ando Kota, my predecessor in the field of droplet research. Your prior work laid the foundation for my research. I want to express my gratitude to the other alumni of the research group. The time we shared, including memorable trips and other leisure activities, have been a source of inspiration. I also want to express my appreciation to Yuta Suzuki for engaging in theoretical discussions. Your willingness to explore new perspectives has enriched the scholarly aspect of my work. To Yuna Aonuma and other students in the lab, I extend my thanks for the collaborative spirit that defined our everyday research life.

Last but certainly not least, I extend my deepest gratitude to my wife, Aiko.

Her understanding and steadfast support allow me to focus on my research. As I embark on the next chapter of my career, I look forward to continuing our journey together. I am grateful once again for her non-oscillating presence in my life.